JOURNAL OF GEOPHYSICAL RESEARCH: ATMOSPHERES, VOL. 118, 1–19, doi:10.1002/jgrd.50782, 2013

Charge rearrangement deduced from nearby electric field measurements of an intracloud flash with K-changes

William W. Hager[1] and Wei Feng[1]

Received 11 January 2013; revised 10 August 2013; accepted 22 August 2013.

[1] An intracloud flash near Langmuir Laboratory is analyzed to determine the net rearrangement of charge. The analysis employed data from a balloon borne electric field sensor, or Esonde, that was within a few hundred meters of the lightning channel, data from a similar Esonde on a mountain about 6.4 km from the balloon, and data from the New Mexico Institute of Mining and Technology Lightning Mapping Array (LMA). The recovery of the charge transport required the solution of Poisson's equation over the mountainous terrain surrounding Langmuir Laboratory and the solution of a vastly under-determined system of equations. The charge movement is analyzed using a new smooth charge transport model that incorporates constraints in the least squares fitting process through the use of penalty terms to smooth the charge movement and prevent data overfitting. The electric field measurements were consistent with about 26% of the negative charge being transported to the end of the channel, 36% deposited along the channel in the positive region, 8% deposited near the start of the channel in the positive region, and 30% deposited in another positive region several kilometers beneath the main channel. The transport of negative charge to a lower positive region occurred during the K-processes when some negative charge was also deposited along the main channel in the upper positive region. Hence, the charge transport process during the K-processes amounted to a *tripolar* charge rearrangement where the charge from the negative region was transported to two distinct positive regions, the positive region along the main channel and a lower positive region beneath the main channel. High altitude, widely scattered LMA sources beyond the end of the main channel could indicate the existence of streamers which transported the end-of-channel charge into the surrounding volume. Although the LMA showed the development of two upper channels, the charge transport analysis showed that measurable charge transport only occurred on one of the channels. The channel that did not transport charge was missing the high altitude, widely scattered LMA sources seen at the end of the channel that carried charge.

Citation: Hager, W. W., and W. Feng (2013), Charge rearrangement deduced from nearby electric field measurements of an intracloud flash with K-changes, *J. Geophys. Res. Atmos.*, *118*, doi:10.1002/jgrd.50782.

1. Introduction

[2] In *Hager et al.* [2007], we analyzed a nine-stroke negative cloud-to-ground flash (CG) near Langmuir Laboratory which discharged a negative region in the cloud between 5 and 8 km in altitude (relative to sea level) on 18 August 2004. We showed that each stroke removed charge from a different region of the cloud, and the discharged regions progressed in a regular pattern through the cloud. Thus, the lightning channel in the CG behaved like a conductor that transported charge between different regions in the cloud and the ground.

[3] In this paper, we focus on charge transport in a normal polarity intracloud flash (IC) that also included K-changes. We will determine the charge rearrangement that occurs during the initial charge transport and during the subsequent K-changes. One goal is to determine to what extent the IC distributes charge along the lightning channel or transports charge to the end of the lightning channel (similar to a CG). A fundamental difference between an IC and a CG is that the channel for a CG is generally located in a single charge region of the cloud, while the channel for an IC connects both a negative and a positive region. When the lightning channel extends into the positive region, the electrons in the channel plasma would be attracted to the surrounding positively charged particles in support of the distributed view of an IC discharge. There is substantial literature in support of the distributed charge model including work by *Few* [1970], *Krehbiel* [1981], *Liu and Krehbiel* [1985], *Proctor* [1981, 1997], *Weber et al.* [1982], and *Lu et al.* [2011]. In particular, *Lu et al.* [2011] propose a time-dependent

[1]Department of Mathematics, University of Florida, Gainesville, Florida, USA.

Corresponding author: W. W. Hager, Department of Mathematics, University of Florida, Gainesville, FL, USA. (hager@ufl.edu)

2169-897X/13/10.1002/jgrd.50782

multidipole model (TDMD) for computing the charge distribution using channel location data from a lightning mapping array and electric field data from an airborne electric field sensor (Esonde). In other recent work by *Hager et al.* [2007, 2010], it was observed that the charge transport in an IC was often closely approximated by a dipole. This paper makes a detailed study of the charge transport and rearrangement in a recently observed IC containing K-changes.

[4] Our analysis is based on data reported by *Winn et al.* [2011] during a thunderstorm near Langmuir Laboratory on 24 August 2007. The electric fields were measured using two Esondes, a balloon borne Esonde, which we refer to as the flight Esonde, and an Esonde on the ground near the Langmuir Laboratory balloon hangar, referred to as the ground Esonde. The flight Esonde, at an altitude of 9100 m in a positive region of the cloud, passed within a few hundred meters of the lightning channel of an IC. The three components of the electric field change near the lightning channel together with the vertical electric field change on the ground is the basis for our charge transport analysis. *Winn et al.* [2011] found that the electric field data of the flight Esonde were consistent with a linear charge density of –0.36mC/m along the lightning channel near the balloon. In this paper, the data from both Esondes are combined to study in more detail the overall charge transport. The analysis is complicated by the geometry: The ground Esonde is located on a mountain at an altitude of 3226 m, and the mountain geometry can effect the electric field measurement by a factor on the order of two, as pointed out in section 3.1 of *Hager et al.* [2012] or section 6.2.1 of *Lu et al.* [2011]. Hence, it is important to consider the three-dimensional geometry of the mountain when utilizing the electric field data.

[5] For many years, ground-based measurements of the change in the electric field under a thundercloud have been used to estimate the location and amplitude of thundercloud charge distributions [*Jacobson and Krider*, 1976; *Koshak et al.*, 1999; *Koshak and Krider*, 1989, 1994; *Krehbiel et al.*, 1979; *Krehbiel*, 1981, 1986; *Murphy et al.*, 1996; *Wilson*, 1916, 1920; *Workman and Holzer*, 1939]. More recently [*Sonnenfeld et al.*, 2006; *Hager et al.*, 2007, 2010; *Lu et al.*, 2011], balloon-based measurements of the change in the electric field have been used in charge retrieval analysis. In our earlier work, the charge transport was fit by a monopole or a dipole, and constraints were incorporated into the retrieval analysis to eliminate degrees or freedom. Constraints include the conservation of charge, a lower bound on the distance between the end of dipoles and location constraints imposed by LMA data.

[6] In this paper, we present a new smooth charge transport model that allows us to analyze in detail the movement of charge during a lightning flash using limited data. The new model constrains the transport to occur in the domain delineated by the LMA, but without monopole or dipole constraints. Instead, the charge transport is constrained to occur in a smooth way. This smoothness in the charge transport parallels the smoothness in charge density seen in balloon soundings of thunderclouds [*Marshall and Rust*, 1991, 1993; *Stolzenburg and Marshall*, 1994; *Stolzenburg et al.*, 1994, 1998a, 1998b, 1998c, 2001, 2002]. The smoothness constraint allows us to fit the vastly under-determined system of equations relating charge to electric field in a physically plausible way.

[7] The paper is organized as follows: In section 2 we give an overview of the balloon flight and the three data sets used in our analysis: radar data, LMA data, and electric field data. In section 3 we explain how the lightning channel was reconstructed, while section 4 explains how we took into account the topography of the earth when computing the electric field from a point charge. Section 5 analyzes the net charge transport, and presents the smooth charge transport model. An analysis of the charge transport during two K-changes is given in section 6. Section 7 summarizes the observations. Appendix A gives more details concerning the numerical approach used to compute the electric field from a point charge.

[8] *Polarity Convention*: The sign convention we employ for the electric field is that it points in the direction of the force exerted on a positive test charge. In the atmospheric electricity community, this is referred to as the physics convention. When reporting our measurements of the vertical electric field, positive electric field points away from the surface of the earth.

[9] *Coordinate System*: Throughout the paper, the coordinates in plots are relative to an origin at sea level directly below a point near the NW corner of the annex building of Langmuir Laboratory. The positive x axis is directed to the east, the positive y axis points to (true) north, and the z axis is vertical, pointing away from the surface of the Earth.

[10] *N3R radar scan*: In the paper, we make reference to N3R radar scans. The label "N3R" is the NEXRAD naming convention for data files associated with radar scans whose angles of tilt are nominally 3.35°.

2. Overview of the Balloon Flight and Data

[11] On 24 August 2007 at about 22:53:51 UT, *Winn et al.* [2011] launched a balloon borne Esonde from the balloon hangar (latitude 33.98210 N, longitude 107.18843 W, altitude 3226 m) near Langmuir Laboratory. A description of the instrument is given in *Winn et al.* [2011, Appendix A]; also see *Sonnenfeld et al.* [2006]. The balloon traveled primarily to the east while ascending to an altitude of 13,307 m before the cutdown package was activated. This detached the balloon from the Esonde, and the instrument with data stored in flash memory, dropped to the ground west of Interstate 25 and the Rio Grande River where it was retrieved at an altitude of 1433 m. At about 23:05:42 UT, 11 min and 50 s after launch, while at an altitude of about 9100 m, the balloon passed within 181 m of an LMA source detected by New Mexico Tech's Lightning Mapping Array (LMA). See *Rison et al.* [1999], *Thomas et al.* [2001, 2004], and *Coleman et al.* [2003] for a description of the New Mexico Institute of Mining and Technology LMA network.

2.1. Radar Data

[12] In Figure 1, we superimpose on the N3R reflectivity plot from the National Weather Service KABX NEXRAD (Albuquerque, NM) all 719 LMA sources for the intracloud flash. The LMA sources first propagate from the initiation point eastward; these initial sources are shown as white dots, and this part of the lightning channel is referred to as channel 1. Then the LMA sources return to the flash initiation point and propagate northward; these later LMA sources are

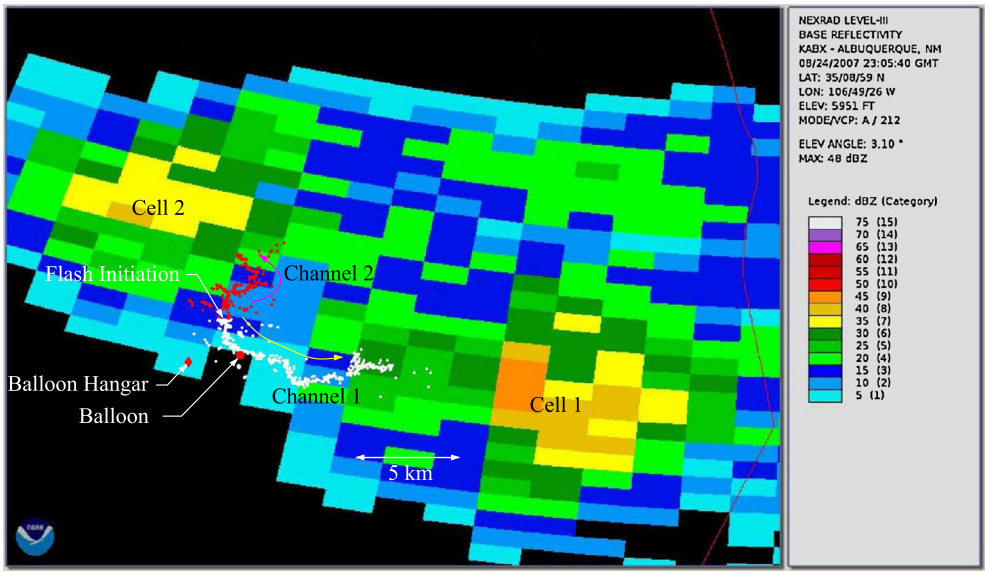

Figure 1. The LMA sources for the intracloud flash superimposed on the N3R reflectivity of National Weather Service Station KABX (Albuquerque, NM) on 24 August 2007 at about 23:05:40 UT. Initially, breakdown progresses eastward (white dots) from the initiation point toward cell 1, then breakdown returns to the initiation point and progresses northward toward cell 2 (red dots). At the time of the flash, the balloon was about 300 m from the lightning channel. The balloon had been launched from the balloon hangar near Langmuir Laboratory about 11 min 50 s earlier.

shown as small red dots, and the corresponding channel is denoted channel 2.

[13] Since the N3R reflectivity plot shows reflection from particles near the top of the cloud, it appears that there were two updrafts in the vicinity of the intracloud flash. Channel 1 propagates toward cell 1 in Figure 1, while channel 2 propagates toward cell 2. The balloon was near channel 1, while the balloon hangar, where the ground Esonde was located, was about 6.4 km southwest of the balloon. The Esonde at the balloon hangar had a balanced view of the entire flash in the sense that it was roughly 6 km from the middle of the flash and less than 15 km from either end.

[14] Since the charged particles in a thunderstorm are generally created in the updrafts, and since the upper regions of the updraft are typically positively charged, the IC breakdown is progressing toward the upper region of the updrafts where a high concentration of positively charged particles is expected. Notice that cell 1 appears to be much more intense and larger than cell 2; cell 1 extends over a larger area with a reflectivity greater than that of cell 2, and the breakdown first propagates to cell 1, even though it was about three times further away from the flash initiation point than cell 2.

2.2. LMA Data

[15] Figures 2–4 show the plan view, the altitude view, the east view, the altitude histogram, and the altitude of the LMA sources as a function of time. The first LMA source was recorded at 23:05:41.917228 UT, while the last source was at 23:05:42.263568 UT. In 2007, the LMA network had to deal with interference from an El Paso television station, and hence the LMA data in that year were noisier than usual. To reduce noise, we restrict our analysis to LMA sources detected by at least eight stations with a chi-squared value less than one. Observe that the LMA sources in the negative region of Figure 3a mostly occurred after channel 1 had been formed. The absence of LMA source in the negative region during the formation of channel 1 indicates that the initial breakdown below 8 km progressed from the positive region down into the negative region. That is, positive polarity breakdown through negative charge is difficult to detect by the lightning mapping array as explained by *Shao and Krehbiel* [1996]. However, after the initial breakdown and charge transport, there were a series of K-changes which produced LMA sources that revealed the location of the negative charge region. In Figure 3, we see that the negative charge region extends between 6 and 8 km altitude, while the positive charge region extends from 8 to nearly 12 km altitude. The three K-changes, or recoil leaders to the positive region, are shown in Figure 4 where we plot altitude of the LMA sources versus time.

[16] About 0.4 s after the last LMA source from the IC, there was another burst of LMA activity which appears as red dots in Figure 4. Altogether, there are 170 new LMA sources, at an average altitude of about 6 km; these were located beneath the earlier LMA sources. In Figure 5, these new LMA sources appear as red dots. Since the electric fields did not jump during the time period of these new sources, the charge transport associated with these late LMA sources was not measurable. Moreover, there is no evidence of a channel in these late sources.

2.3. Electric Field Data

[17] The electric field measured by the flight Esonde and the ground Esonde near the Langmuir Laboratory balloon hangar are shown in Figure 6. The recovery of the electric fields from the Esonde measurements of induced charges on four metal plates is not easy. The fields shown in the figures were obtained using an algorithm developed in *Hager et al.*

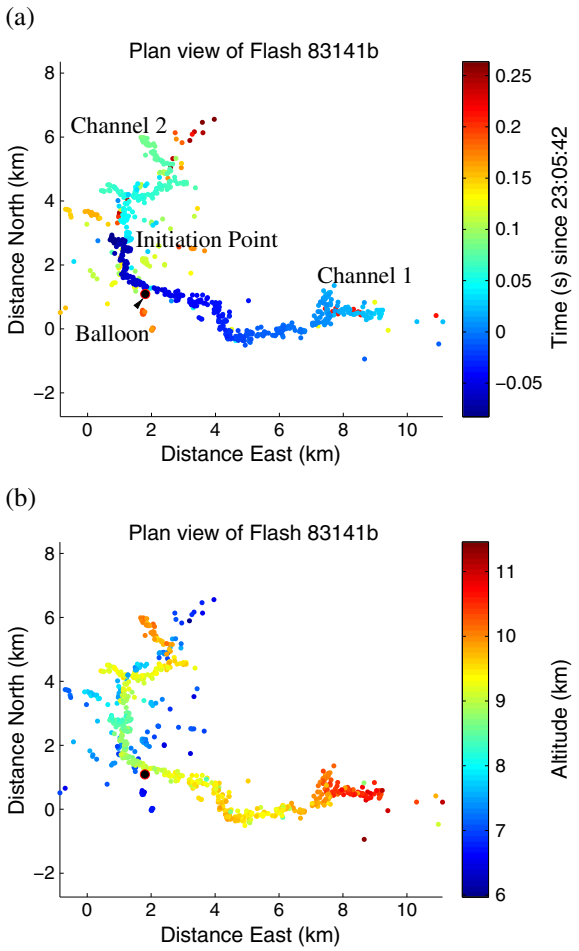

Figure 2. (a) Plan view of the LMA sources, depicted as dots, in the Langmuir Laboratory coordinate system. The color of the dots is based on the time since the start of the flash; the first LMA sources are colored dark blue while the last are dark red. The balloon appears as a large black dot with a red edge. Channel 1 propagates toward cell 1 in Figure 1 while channel 2, which develops later in the IC, propagates toward cell 2. (b) The same view of the LMA sources but with the dot color based on the altitude of the source. The low altitude LMA sources in the negative region are blue while the higher sources in the positive region are green, yellow, and red.

[2010] that exploits the instrument rotation in order to estimate the x and y components of the electric field. Since we can only measure the electric field *change* in the z direction, E_z is initialized to zero at the start of the flash. During the 300 ms of the flash, the flight Esonde rotated 24°. This was sufficient rotation to recover both the x and y components of the electric field. Hence, the initial x and y components of the electric field in Figure 6 are nonzero, and correspond to their true values.

[18] In Figure 6, the dashed vertical lines show the time of the first LMA source of the flash, and the time, denoted t_0, when the LMA sources reached the end of channel 1. In section 5, we reconstruct on the charge transport between t_0 and a time t_2 after the flash is complete, while section 6 focuses on the charge transport during the K-changes, the small steps seen in the electric field between 23:05:42.1 and 23:05:42.3 in Figure 6.

[19] Between the dashed lines in Figure 6, E_y increases as the LMA sources approach the balloon, and then decreases after the LMA sources have gone past the balloon; E_x decreases as the LMA sources approach, and then increases after the LMA sources have gone past the balloon—see Figures 1 and 2 for the location of the balloon. As noted by *Winn et al.* [2011], this behavior for the electric field corresponds to a negative current wave traveling down channel 1 and passing the balloon. In *Winn et al.* [2011], it is shown that the oscillations in the electric field seen immediately after the peak in the electric field amplitude corresponds to recoils produced by the growth of the stepped leader.

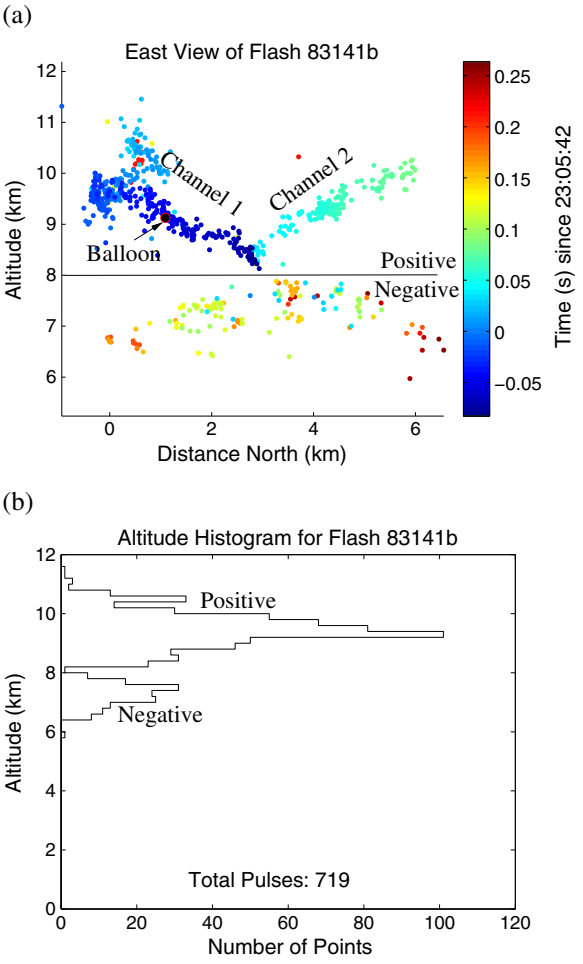

Figure 3. (a) A view of the LMA sources from the west, looking east. Channel 1 appears on the left side, while channel 2 appears on the right. The part of the plot labeled "Negative" indicates the region where most of the negative charge was located. The charge transport analysis later reveals a pocket of positive charge beneath channel 1. (b) The histogram counts the number of LMA sources in 200 m thick horizontal slices through the cloud. Again, most of the LMA source beneath 8 km were located in a negatively charged region, while a pocket of positive charge was also found beneath 8 km altitude.

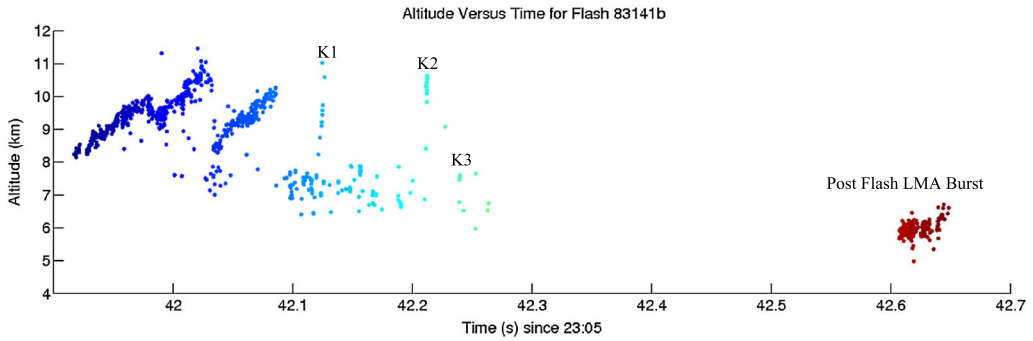

Figure 4. Altitude of the LMA sources as a function of time. The third K-change, K3, barely reaches the positive region.

3. Channel Reconstruction

[20] In order to reconstruct the charge transport, we first reconstruct the lightning channel. In *Hager et al.* [2007], we explain how to construct the pulse graph of a flash. The algorithm provides a systematic way of connecting the LMA sources in a flash in order to obtain a graphical approximation to the lightning channel. The pulse graph was used in *Hager et al.* [2007, 2010] to compute a dipole approximation to the charge transport in an IC. In this paper, we consider distributed charge transport, where the pulse graph seems inappropriate since it could connect LMA sources on numerous short side channels while missing the main channel. Our goal now is to compute a relatively smooth one-dimensional curve in three-dimensional space that in some sense passes through the middle of the LMA data. Our algorithm for building the channel is the following:

[21] 1. Extract the LMA sources in the general location of the channel. For example, to reconstruct channel 1, we could start with all the white sources in Figure 1 with altitude greater than 8 km. We need to initialize the algorithm with the location of the start of the channel and a direction vector pointing along the channel. Let p_1 and d_1 denote this starting point and direction. Next, we choose the length ℓ of the reconstructed channel segments, and the radius r of a sphere in which we will analyze the LMA data. In our channel reconstruction, we take $\ell = 100$ m for the channel segments and $r = 750$ m for the radius of the sphere. Finally, we initialize $k = 1$.

[22] 2. Assuming the kth point p_k on the channel and the channel direction d_k are known, the $(k + 1)$st point p_{k+1} and the corresponding direction d_{k+1} are determined as follows: We extract all the LMA points in the intersection of the sphere of radius r centered at p_k with the half-space passing through p_k with inward normal d_k. Let H be the LMA sources contained in both the sphere and the half-space. For any direction vector d emanating from p_k, we evaluate the sum of the distances of the LMA sources in H to the direction d. d_{k+1} is the unit vector associated with the direction that minimizes the sum of the distances and $p_{k+1} = p_k + \ell d_{k+1}$. As the channel reconstruction proceeds, we discard the points contained in previous spheres which are outside of the current sphere; hence, we eventually run out of points. Plots showing the reconstructed channels appear in Figure 7.

[23] Our choices for the sphere radius r and the length ℓ of the channel segments were based on the following considerations: Since the LMA sources are spread out spatially around the channel, the radius of the sphere r should be several times the spatial spread. Since the spatial spread is on the order of 100 to 200 m, $r = 750$ is large enough to get past the spread and determine the channel direction. The length ℓ of the channel segments was chosen to approximate the length of the channel segments associated with the stepped leader. Since lightning builds its channel in segments that vary from 10 to 200 m in length (see *Rakov and Uman* [2003, p. 131]

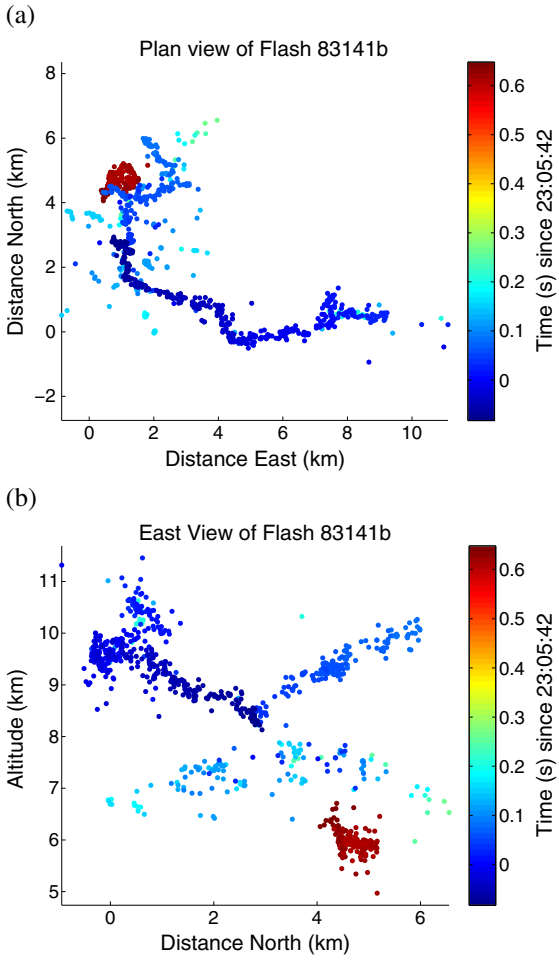

Figure 5. (a) Plan view of the LMA sources, including the late, low altitude LMA sources in red that appeared about 0.4 s after the completion of the IC.(b) The view of the LMA sources from the west looking toward the east.

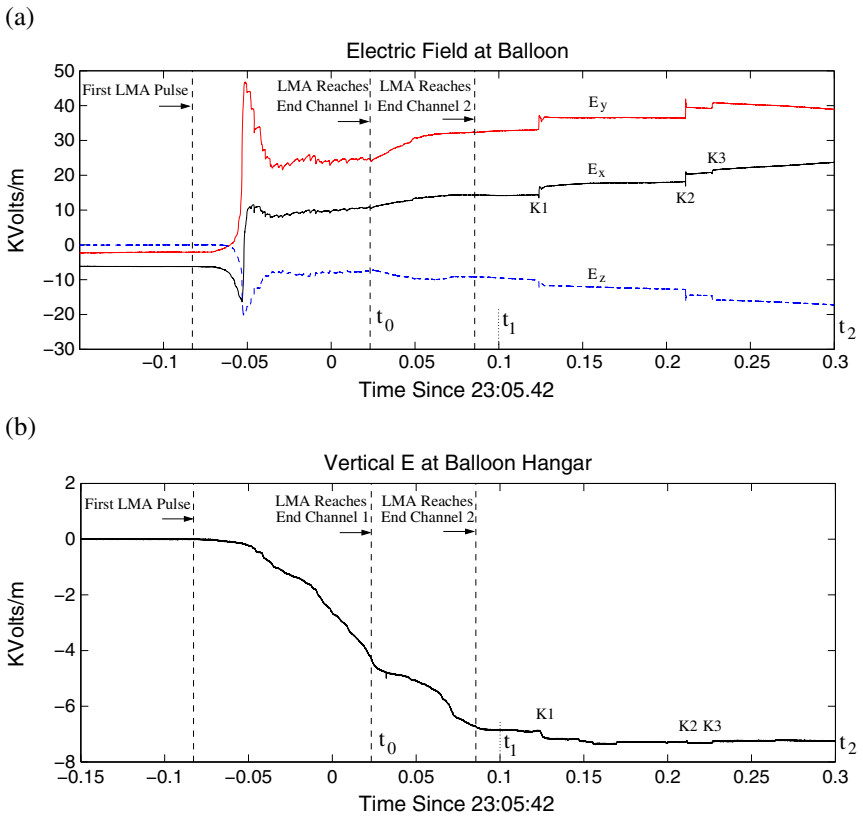

Figure 6. (a) The electric field at the flight Esonde during the flash of 23:05:42 UT. The first dashed vertical line shows the instant of time when the first LMA source was recorded, while the second dashed vertical line shows the time, denoted t_0, that the LMA sources reached the end of channel 1. The charge transport at t_0 as well as at the later times t_1 and t_2 will be studied in this paper. The first LMA source of channel 2 occurs when the LMA sources reach the end of channel 1 (time t_0). Three K-changes, the small steps in the electric field, are labeled on the plot of E_x. These occur between time t_1 and t_2. (b) The electric field at an Esonde hanging 1 m above the ground near the Langmuir Laboratory balloon hangar.

where work of *Schonland* [1956] is cited), 100 m seemed like an appropriate length for the channel segments.

4. Electric Field Analysis for Point Charge

[24] For our flash, the analysis of the electric field from a point charge is complicated by the mountain on which Langmuir Laboratory is situated. As noted by *Hager et al.* [2012] and *Lu et al.* [2011], the mountain geometry can strengthen the electric field by a factor on the order of 2. Hence, in order to correctly interpret the electric field data from the two Esondes, one on the mountain and the other in the air, it is important to take into account the geometry of the mountain.

[25] The electrostatic relationship between charge and field is governed by Poisson's equation

$$\epsilon_0 \nabla^2 V = -\rho \quad \text{on} \quad \Omega,$$

where V is the electric potential, ∇^2 is the Laplacian, ϵ_0 is the permittivity of free space, ρ is charge density, and Ω is the domain where we wish to solve for the potential. The electric field is the negative gradient of potential: $E = -\nabla V$. Poisson's equation by itself does not uniquely determine V. In addition, V must satisfy conditions on the boundary of Ω, often denoted $\partial\Omega$.

[26] If we were computing the electric potential associated with the thunderstorm, then appropriate boundary condition far from the storm could be the fair field potential on the vertical sides of the domain and the ionospheric potential above the storm [*Adlerman and Williams*, 1996]. In our case, on the other hand, we are not interested in the potential for the entire storm, we are interested in the potential change associated with the insertion of a point charge in the atmosphere. Hence, we need to solve Poisson's equation when ρ is replaced by a delta function corresponding to a point charge. The appropriate boundary conditions are simply the homogeneous boundary conditions: the potential should vanish on the surface of the earth, at the ionosphere, and at distant locations far from the point charge; in particular, we set V to zero 100 km away from the point charge. These boundary conditions are approximations since the earth and the ionosphere are not perfect conductors, and the distant potential is not zero, but decays like the reciprocal of distance. Nonetheless, the errors due to our approximations to the true boundary conditions are relatively small compared to the uncertainty in the data.

[27] In implementing the homogeneous boundary condition on the surface of the earth, we used the 1/3 arc-second elevation data available from the U.S. Geological Survey at the Web site nationalmap.gov. This data roughly corre-

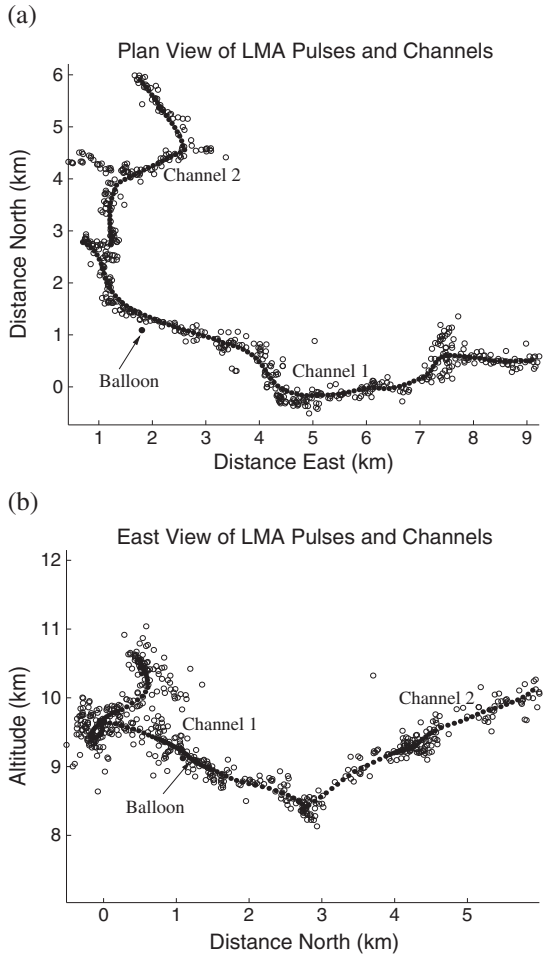

Figure 7. (a) The plan view of the LMA sources (empty circles) and the reconstructed channel (filled circles) corresponding to the negative stepped leader in the positive region. (b) A view from the west side of the flash, looking east, of the LMA sources and the reconstructed channel.

sponds to elevations on a 10 m by 10 m grid over the surface of the United States. The distance from the surface of the earth to the center of the earth was 6378135 m (the approximate radius of the earth) plus the elevation given by the U.S. Geological Survey.

[28] In order to model the charge transport, we placed delta function charges at the midpoints of the 100 m segments forming the lightning channel. If we numerically solve Poisson's equation with a delta function right side, then there are often substantial errors in the numerical solution due to the singularity in the potential at the location of the delta function. In order to compute the solution with greater accuracy, we exploited the fundamental solution for Laplace's equation on the exterior of a sphere:

$$V_f(P) = \frac{1}{4\pi\epsilon_0}\left\{\frac{1}{\|P-P_0\|} - \frac{R/\|P_0\|}{\|P-(R^2/\|P_0\|^2)P_0\|}\right\},$$

where P_0 is the location of the delta function, P is the point where the potential is measured, and R is the radius of the sphere where V_f should vanish. We chose R to be the mean elevation of the surface of the earth over Ω. This fundamental solution has the property that it vanishes on the sphere of radius R and its Laplacian (times ϵ_0) is a delta function concentrated at P_0. If ρ is this delta function, then the solution to Poisson's equation can be expressed as $V = V_f + V_0$, where $\nabla^2 V_0 = 0$ and $V_0 = -V_f$ on $\partial\Omega$. Since V_f vanishes at the mean elevation of the earth over Ω, V_f is relatively small over the surface of the earth, which implies that the boundary conditions for V_0 are relatively small. Hence, we are able to express V as the sum of the known singular fundamental solution V_f and an unknown, smooth function V_0 satisfying Laplace's equation with relatively small boundary conditions. Since V_0 is smooth, we can compute it accurately, and hence, we obtain an accurate representation of V. The electric field is expressed as $E = -(\nabla V_f + \nabla V_0)$, where ∇V_f is computed analytically while ∇V_0 is computed numerically.

5. Net Charge Transport Analysis

[29] In this section we determine the charge transport associated with the electric field data in Figure 6. Before presenting our new smooth charge transport model, we first examine some simpler models to understand their limitations. Initially, let us focus on the charge transport from the beginning of the flash up until either 23:05:42.1 UT (denoted t_1) or 23:05:42.3 UT (denoted t_2)—see Figure 6. At both these times, the electric field is relatively stationary. t_1 occurs after the LMA reach the end of channel 1, but before the start of the K-processes. t_2 occurs after the completion of the flash.

5.1. Dipole Charge Transport Model

[30] As mentioned in the introduction, dipole models often provide good approximations to the charge transport in an IC. In this model, negative charge is transported from the negative region and deposited near the ends of the channels. Let us suppose that a charge Q_1 is deposited at a location 700 m from the end of channel 1, and another charge Q_2 is deposited at a location 700 m from the end of channel 2. The origin of the charge will be the negative region indicated in Figure 3. More precisely, we suppose that the total charge $Q_1 + Q_2$ originated from locations coinciding with each of the LMA sources in the negative region. An equal amount of charge is assigned to each LMA source location. By conservation of charge, we deduce that the number of LMA sources in the negative region times the charge at each location has the same magnitude as the total charge transport Q_1+Q_2. The charges Q_1 and Q_2 are chosen to give the best least squares fit to the measured data. The values of Q_1 and Q_2 and the comparison between modeled and measured data are shown in Table 1.

[31] Here F and G stand for flight and ground respectively, and EG is the electric field at the ground Esonde, for example. Clearly, this fit is nonsense! The modeled Q_1 is

Table 1. Dipole Charge Transport Model

	t_1 = 23:05:42.1 UT		t_2 = 23:05:42.3 UT	
	Measured	Modeled	Measured	Modeled
EG_z (kV/m)	–6.8	5.5	–7.2	5.0
EF_x (kV/m)	20.4	–7.0	29.9	–8.1
EF_y (kV/m)	35.0	22.6	41.1	25.6
EF_z (kV/m)	–9.4	–11.3	–17.1	–18.7
Q_1 (C)		31.2		28.1
Q_2 (C)		–31.1		–27.9

Table 2. Uniform Charge Transport Model

	t_1 = 23:05:42.1 UT		t_2 = 23:05:42.3 UT	
	Measured	Modeled	Measured	Modeled
EG_z (kV/m)	–6.8	–3.4	–7.2	–1.8
EF_x (kV/m)	20.4	24.1	29.9	31.7
EF_y (kV/m)	35.0	33.1	41.1	40.9
EF_z (kV/m)	–9.4	–6.8	–17.1	–14.4
Q_1 (C)		–7.7		–10.3
Q_2 (C)		0.1		7.0

positive when it should be negative, the x component of the modeled electric field is negative when it should be positive, and the z component of the modeled electric field on the ground is positive when it should be negative. Thus, transport of the charge to points near the end of the channels provides extremely poor agreement with the data, even for the best possible choices of Q_1 and Q_2. The reason that the end-of-channel model did not work was that the flight Esonde was near the channel, and the nearby charge on the channel had a significant impact on its charge measurement. Unless we put charge along the channel, we are not able to match the electric field at the flight Esonde.

5.2. Uniform Charge Transport Model

[32] Next, let us consider a uniformly distributed charge on each channel. At the centroid of each segment of channel 1, we place an equal amount of charge q_1. Similarly, at the centroid of each segment of channel 2, we place an equal amount of charge q_2. Finally, at the location of each LMA source in the negative region, we place an equal amount of charge q_- which is determined by conservation of charge. If Q_1 and Q_2 denote the total amount of charge on channels 1 and 2, respectively, then the best least squares fit between the modeled and measured data are shown in Table 2.

[33] The uniformly distributed charge model was a better fit to the data; however, the small positive charge along channel 2 at t_1 seems peculiar. At t_2, the total charge along channel 2 has become an implausible 7.0 C, meaning that 7.0 C positive charge was deposited on the channel in the positive region. The fit to the ground electric field is in error by a factor of 2 at t_1 and by a factor of 4 at t_2. Thus, the uniformly distributed charge model also fails to reproduce the measured electric field, even for the best possible choices of q_1, q_2, and q_-. This indicates that the charge is not uniformly distributed along the channel, and that greater flexibility in the charge deposition is needed in order to reproduce the measured electric fields.

5.3. Smooth Charge Transport Model

[34] In section 3, we developed an approximation to the lightning channels for our flash using 152 channel segments. Since the charge on each of these 152 channel segments is unknown, we have 152 degrees of freedom that could be used to fit the measured electric field at any instant of time. Since there are only four data constraints corresponding to the three components of the electric field change at the Esonde and the vertical electric field change on the ground, we have a vastly under-determined system of equations. If we do not remove degrees of freedom, then we are in danger of "overfitting" the data. That is, we can match the measurement very precisely using charge distributions that have no physical significance. In the previous subsections, we removed degrees of freedom by assuming the charge distribution had very special forms. In the dipole fit, we assumed that the charge on all the channel segments was zero except for the charge on a segment near the end of each channel. In the uniform fit, we assume that the charge on each channel segment was the same. Either of these models removed nearly all the degrees of freedom, but there was a significant discrepancy between the electric fields produced by the model and the measured fields. We now develop a completely different way to remove the degrees of freedom, while preserving the flexibility that is needed to match the measured electric fields.

[35] We call our new approach, the "smooth charge transport model," since we try to fit the measured electric field using a charge distribution along the channel that is a smooth, slowly varying function of distance along the channels. This requirement of smoothness eliminates many degrees of freedom and leads to a fit with physical plausibility. At any instant of time, let q_i denote the charge placed on the ith channel segment. Smoothness is achieved by keeping the change $|q_{i+1}-q_i|$ in the charge between two adjacent channel segments small. In the uniform charge transport model, we make this change zero, but found that we were not able to reproduce the observed electric fields with this requirement. We will now use a penalty approach to keep this difference small, but not zero. As a result, we are better able to fit the observed electric fields. In addition to keeping the charge change small between adjacent channel segments, we also incorporate the following constraints:

[36] (C1) We will try to keep the total charge transport small since fits to the data that require huge amounts of charge transport are often mathematical fits that match the data but without physical significance.

[37] (C2) In the region beneath 8 km, we will treat each LMA source as a charge location and we will try to keep the charge amplitude uniform in the negative region. The altitude LMA plot in Figure 2b seems to indicate that the negative region is highly branched; since there are a small number of LMA sources associated with each branch, we simply treat each LMA source in the negative region as the location of a small channel segment, and we will try to keep the charge on each of these channel segments relatively constant.

[38] (C3) In the positive region, near the ends of the channels, we include a constraint $q_{i+1} \leq q_i$. This constraint was suggested by Edward Mansell who pointed out that in the numerical simulations of *Mazur and Ruhnke* [1998], the modeled charge density decreased along the channel. Without this constraint, we found that the charge density could drop to the nonphysical value of 0 several kilometers from

Table 3. Smooth Charge Transport Model ($\ell = 0$)

	t_1 = 23:05:42.1 UT		t_2 = 23:05:42.3 UT	
	Measured	Modeled	Measured	Modeled
EG_z (kV/m)	–6.8	–6.7	–7.2	–6.9
EF_x (kV/m)	20.4	20.4	29.9	30.0
EF_y (kV/m)	35.0	35.0	41.1	42.3
EF_z (kV/m)	–9.4	–9.1	–17.1	–13.6
Q_1 (C)		–15.0		–13.1
Q_2 (C)		–0.2		–1.8

the end of the channel. When this constraint is imposed on the entire channel (instead of just at the ends of the channel), we obtained fit errors between 2% and 5%, which are quite reasonable; however, the recovered charge density exhibited some nonphysical characteristics. For example, the charge density can become completely constant on the channel without any growth at all near the end of the channel where end-of-channel streamers should effectively yield an increased charge density.

[39] The least squares problem that embodies all our constraints is the following:

$$\begin{aligned}\min\ & 3(\mathrm{EG}^{\mathrm{modeled}} - \mathrm{EG}^{\mathrm{meas}})^2 + \|\mathrm{EF}^{\mathrm{modeled}} - \mathrm{EF}^{\mathrm{meas}}\|^2 + p_+ \sum_i q_i^2 \\ & + \sum_{i\in \mathrm{ch1}} p_i (q_{i+1} - q_i)^2 + \sum_{i\in \mathrm{ch2}} p_i (q_{i+1} - q_i)^2 + p_- \sum_{i\in \mathrm{neg}} (q_i - \bar{q}_-)^2 \\ \text{subject to } & \sum_{i\in \mathrm{ch1}} q_i + \sum_{i\in \mathrm{ch2}} q_i + \sum_{i\in \mathrm{neg}} q_i = 0, q_i \le 0, \quad i \in \mathrm{ch1} \cup \mathrm{ch2}, \\ & q_i \ge \ell_i, \quad i \in \mathrm{neg}, q_{i+1} \le q_i \text{ for } i \text{ near ends of channels.}\end{aligned} \tag{1}$$

Here *EF* is the vector electric field at the flight Esonde, $\|\cdot\|$ is the Euclidean norm, and EG is the (scalar) vertical electric field at the ground Esonde. When we compare the modeled and measured electric field, we need to give equal importance to the ground and the balloon borne Esondes. Hence, we weighted the least squares difference between the modeled and measured electric field at the ground by a factor of 3 in (1). In (1), q_i for "$i \in$ ch1" refers to the parcels of charge placed at the midpoint of segments forming channel 1, q_i for "$i \in$ neg" refers to the parcels of charge placed at the location of LMA sources below 8 km, and $\bar{q}_-$ denotes the mean value of charge below 8 km. The constraint

$$\sum_{i\in \mathrm{ch1}} q_i + \sum_{i\in \mathrm{ch2}} q_i + \sum_{i\in \mathrm{neg}} q_i = 0$$

represents conservation of charge. The constraint $q_{i+1} \le q_i$ near the ends of the channels corresponds to the observations of *Mazur and Ruhnke* [1998]. The constraint $q_i \le 0$ for $i \in \mathrm{ch1} \cup \mathrm{ch2}$ implies that we only deposit negative charge in the upper positive region. The charge movement below 8 km altitude, however, is more subtle. During the initial charge transport, it appears that negative charge is extracted from the negative region and deposited in the positive region; hence, $\ell_i = 0$ and we constrain $q_i \ge 0$ for $i \in$ neg. However, after the initial charge transport, we find that charge is mostly rearranged in the region beneath 8 km altitude. This means that $q_i > 0$ where the negative charge is removed and $q_i < 0$ where the negative charge is deposited. To permit a rearrangement of charge in the negative region, we either set $\ell_i = -\infty$ or ℓ_i = a negative number consistent with the amount of charge rearrangement, as will be explained later.

[40] The term $p_i(q_{i+1} - q_i)^2$ only vanishes when $q_{i+1} = q_i$. Hence, this term, which creates the smoothness in our model, keeps the change $q_{i+1} - q_i$ in charge between adjacent channel segments small. Increasing p_i forces q_i and q_{i+1} to approach each other. Since the electric field measured by the flight Esonde is very sensitive to the charge placed on the nearby channel, we want q_i constant along channel segments near the Esonde. There is simply not enough information in the four values of the electric field to determine more than the constant charge density along the channel near the flight Esonde. This requirement is enforced by taking p_i really big when q_i is near the Esonde.

[41] The term $(q_i - \bar{q}_-)^2$ for "$i \in$ neg" only vanishes when q_i = the mean charge $\bar{q}_-$ in the negative region. Since we have limited information concerning the origin of the negative charge other than the LMA source below 8 km altitude, we penalize the deviation of the charge removal at each LMA source location from the mean; in other words, we try to keep the charge removal at each LMA source location in the negative region relatively constant.

[42] In fitting the charge transport to the measured electric field, the penalty parameters were chosen as follows:

[43] (P1) $p_i = 10^{12}$ when q_i is near flight Esonde (charge constant near Esonde)

[44] (P2) $p_i = 10^5$ when q_i is far from flight Esonde (penalty for charge change)

[45] (P3) $p_+ = 10^4$ (penalty for charge deposition)

[46] (P4) $p_- = 10^6$ (penalty for deviation of charge from mean in negative region)

[47] More precisely, we apply the large (P1) penalty along the 1.4 km of channel segments to the west and north of the Esonde and along the 4.9 km of channel segments to the east and south of the Esonde. The optimization is relatively insensitive to these penalty parameter as long as we keep the penalty (P1) for charge variations near the flight Esonde much larger than the other penalties (P2), (P3), and (P4).

[48] The penalties (P1) and (P2) basically control the stiffness in the charge deposition curve along the channel. When p_i is huge, the charge deposition curve is very stiff in the sense that $q_{i+1} \approx q_i$. As p_i decreases, we allow more flexibility in the approximating curve. $p_i = 10^5$ and $p_i = 10^{12}$ both correspond to a rather stiff approximating curve. Taking $p_i = 10^{12}$ for channel segments near the balloon means that the q_i curve is essentially constant, while away from the balloon, $p_i = 10^5$ implies that we allow more flexibility in the curve.

[49] In Table 3, we compare the measured fields at t_1 and t_2 to the modeled fields that are obtained when we solve the penalized least squares problem. Here Q_1 is the total charge on channel 1 and Q_2 is the total charge on channel 2. As can be seen, the fit between modeled and measured fields is almost perfect at t_1. At t_2, the relative error in the fit increased from 1% to 7% where the relative error is the norm of the modeled *E* minus the measured *E* over the norm of the measured *E*.

[50] Since Q_2 is small compared to Q_1, there seems to be very little charge transport on channel 2. In fact, the charge deposit Q_2 on channel 2 was on channel segments very close to channel 1. Hence, the charge transport analysis implies that there was barely any charge transport along channel 2, and the –1.8 C given in Table 3 at t_2 actually represents charge deposited on channel 1. Mathematically, there was a tiny improvement in the fit by moving the charge from channel 1 to a nearby location at the start of channel 2. For bookkeeping purposes, we feel that this charge placed at the start of channel 2 should be associated with the nearby channel 1. In the smooth charge transport model, we can force all the charge to be deposited on channel 1 by setting $p_i = 10^{12}$ when $i \in$ ch2.

[51] As pointed out above, the fit at t_2 was not as good as the fit at t_1. Much of the error occurs in the vertical elec-

Table 4. Smooth Charge Transport Model (at t_2, $\ell_i = -0.06$ for $i \in$ neg)

	t_0 = 23:05:42.023 UT		t_1 = 23:05:42.1 UT		t_2 = 23:05:42.3 UT	
	Measured	Modeled	Measured	Modeled	Measured	Modeled
EG_z (kV/m)	–4.2	–4.2	–6.8	–6.7	–7.2	–7.0
EF_x (kV/m)	16.8	16.8	20.4	20.4	29.9	30.0
EF_y (kV/m)	26.9	26.9	35.0	35.0	41.1	41.3
EF_z (kV/m)	–7.4	–7.6	–9.4	–9.1	–17.1	–16.4
Q_1 (C)		–9.7		–15.4		–15.6
$\|Q_-\|$ (C)		9.7		15.4		22.4

tric field. In particular, the modeled vertical electric field –13.6 kV/m at the Esonde needs to be increased by about 26% to match the measured electric field –17.1. This difference occurs after the K-changes occur, and indicates a fundamental difference in the charge movement during the K-change. We have found that the discrepancy between the modeled and the measured fields can be removed if the constraint $q_i \geq 0$ for $i \in$ neg imposed on the charge transport is relaxed to $q_i \geq \ell_i$ for $i \in$ neg where $\ell_i < 0$. In the next section, we analyze the K-changes in detail and find that $\ell_i = -0.06$ C seems sufficient. This change allows a charge rearrangement beneath 8 km altitude as well as transport down channel 1. When charge is moved from one location to another beneath 8 km altitude, q_i is positive for one i but negative for another i and the constraint $q_i \geq 0$ for $i \in$ neg is no longer satisfied. In other words, at t_2 after the K-changes, we need to take $\ell_i < 0$ in (1) for $i \in$ neg. Note that we could completely eliminate the lower bound by taking $\ell_i = -\infty$ for $i \in$ neg and not much would change. The lower bound –0.06 C is small enough to accommodate the charge rearrangements seen in a K-change.

[52] The electric field change provides strong evidence of the charge rearrangement taking place between t_1 and t_2 in the region labeled "Negative" in Figure 3a. During this time interval, most of the change in the electric field at the flight Esonde occurred in the x and z components with the z component of E decreasing and the x component increasing. The decrease in E_z corresponds to negative charge being placed beneath the Esonde. In contrast, negative charge placed at the end of channel 1 increases E_z since the end of channel 1 is 2 km above the balloon. If negative charge is placed beneath the Esonde, then we need to relax the constraint $q_i \geq 0$ for $i \in$ neg since this constraint only allows us to put positive charge in the region beneath the Esonde.

[53] We now repeat the charge retrieval analysis with $p_i = 10^{12}$ for $i \in$ ch2 and at t_2, $\ell_i = -0.06$ C for $i \in$ neg. We also introduce one more time of interest: t_0 = 23:05:42.023243 UT, which is the time that the LMA sources first reached the end of channel 1. The fit between modeled and measured electric field is shown in Table 4. The relative fit errors are now 1% at all times. In Table 4, we list the quantity $|Q_-|$ which represents the magnitude of the total charge transport in the negative region. At t_0 or t_1, we have $|Q_-| = |Q_1|$ since all the charge was transported from the negative to the positive region. At t_2, we have

$$|Q_-| = \sum_{i \in \text{neg}} |q_i| = 22.4 \text{ C},$$

which is the sum of the charge transport $Q_1 = -15.6$ from the negative to the positive region, and –6.8 C that moved to a different location beneath 8 km altitude.

[54] Earlier we noted that the charge transport analysis did not show measurable charge transport along channel 2. To assess whether this observation is statistically significant, we now study the sensitivity of the electric field measurements to charge deposition on channel 2. If 1 C negative charge is placed at the midpoint of channel 2, then the change in the electric field is $\Delta E = (69, 859, 98)$ V/m at the flight Esonde and $\Delta E_z = 424$ V/m at the ground Esonde; these four numbers should be added to the four modeled fields in Table 4 to obtain the total electric field corresponding to an additional 1 C negative charge on channel 2 along with the charge deposition generating Table 4. Notice that when this negative charge is placed on channel 2, all four components of the modeled electric field at t_1 (an instant of time after the LMA sources reach the end of channel 2) move away from the measured electric fields. In particular, if 10, 5, or 2 C negative charge were placed at the midpoint of channel 2, then the corresponding relative errors in the modeled electric field at the ground Esonde are 63%, 33%, and 14% respectively. Since the total charge transport was 22.4 C, we conclude that relatively small amounts of charge placed on channel 2 are easily detected and have a significant input in the analysis. Since any charge that we put on channel 2 seems to move the modeled fields away from the measured data, the data does not support measurable charge transport on channel 2.

[55] The fit between the modeled and measured electric fields is shown on the entire interval $[t_0, t_2]$ in Figure 8. Since we are estimating the charge deposition on the entire channel, the plot starts at t_0, when the LMA sources first reach the end of channel 1. An analysis of the charge deposition before t_0 would require an estimate for the location of the leader tip from the LMA data; the fit process at any instant of time would then be restricted to the existing ionized channel. See *Winn et al.* [2011, Figure 6] for a model of the current wave associated with the stepped-leader phase of the flash.

[56] The error in the modeled electric fields in Figure 8 is largest at t_2, the end of the flash. The relative error in the modeled electric field at the ground is about 3% while the error in the modeled z component of the electric field at the Esonde is about 4%. The errors in the modeled x and y components of the electric field at the Esonde are less than 1%.

[57] The charge transport along channel 1 as a function of distance along the channel is shown in Figure 9 where we plot linear charge density in mC/m (millicoulombs per meter). The least squares fit yields the charge at the midpoint of each 100 m channel segment; we divide by 100 to obtain the charge per meter (linear charge density) on that channel segment. Observe that between t_0 and t_2, the charge tends to move down the channel. There is a hump in charge density

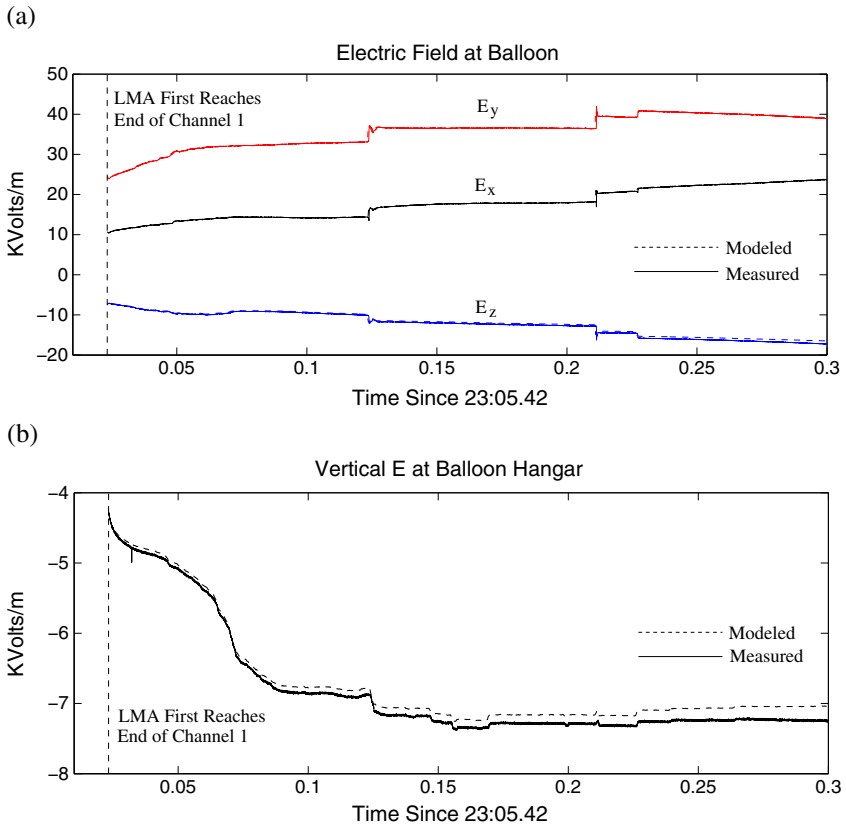

Figure 8. Comparison between modeled and measured electric fields (a) at the Esonde and (b) at the balloon hanger. The relative error in the model is 3% in Figure 8b, while in Figure 8a, the relative error in the model is 4% for E_z and less than 1% for E_x and E_y. The largest relative errors are found by comparing the last two columns of Table 4.

near the start of channel 1. The hump is smallest at t_0, largest at t_1, and intermediate at t_2. The accumulation of charge at the end of channel 1 increases with time. The large charge densities at the start and end of channel 1 do not necessarily imply that there was a high concentration of charge on the channel. Instead, the charge could propagate into the surrounding atmosphere, and the computed channel charge is a centroid for the charge transported into the surround atmosphere.

[58] The geometry of the charge transport process could contribute to the charge bulge near the start of channel 1. In this flash, a volume of negative charge several kilometers in diameter feeds a channel in the positive region whose conducting core is possibly 1 to 2 cm in diameter, as estimated in *Rakov and Uman* [2003, p. 7]. Although the channel conductivity is huge, it is still finite, and the difference between the rate of charge flow up to the start of channel 1 and the rate of charge flow along channel 1 could cause some charge accumulation near the start of the channel. The charge bulge is largest at time t_1, an instant of time after the LMA sources reach the end of channel 1, but before the K-changes.

[59] Near the balloon, the linear charge density was about –0.55 mC/m at t_0, –0.69 mC/m at t_1, and –0.90 mC/m at t_2. These charge densities are greater in magnitude than the –0.36 mC/m density reported by *Winn et al.* [2011]. The difference may be connected with channel location. *Winn et al.* [2011] used 200 m for the distance between the balloon and the lightning channel. Although the distance from the balloon to the closest LMA source was 181 m, our channel location was taken as 304 m from the balloon based on the least squares fit to the channel described in section 3. Since our channel is located at a greater distance from the balloon than in *Winn et al.* [2011], more charge must be placed on the channel to fit the measured electric field.

[60] In Figures 10 and 11, we plot the locations in the region beneath the 8 km altitude where negative charge was removed or deposited. The area of each circle is proportional to the charge magnitude, and the center of each circle is an LMA source. The circle is filled if negative charge was removed; the circle is open if negative charge was deposited. In Figures 10a, 10b, 11a, and 11b, which correspond

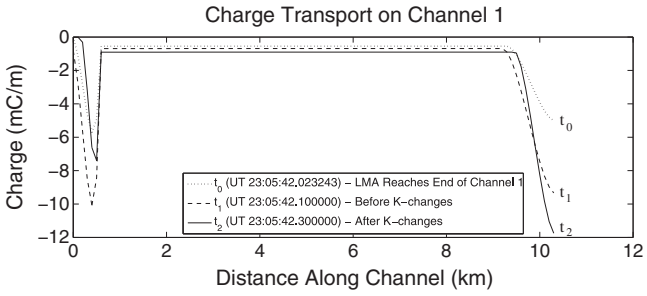

Figure 9. Linear charge density on channel 1 as a function of distance along the channel at three different times.

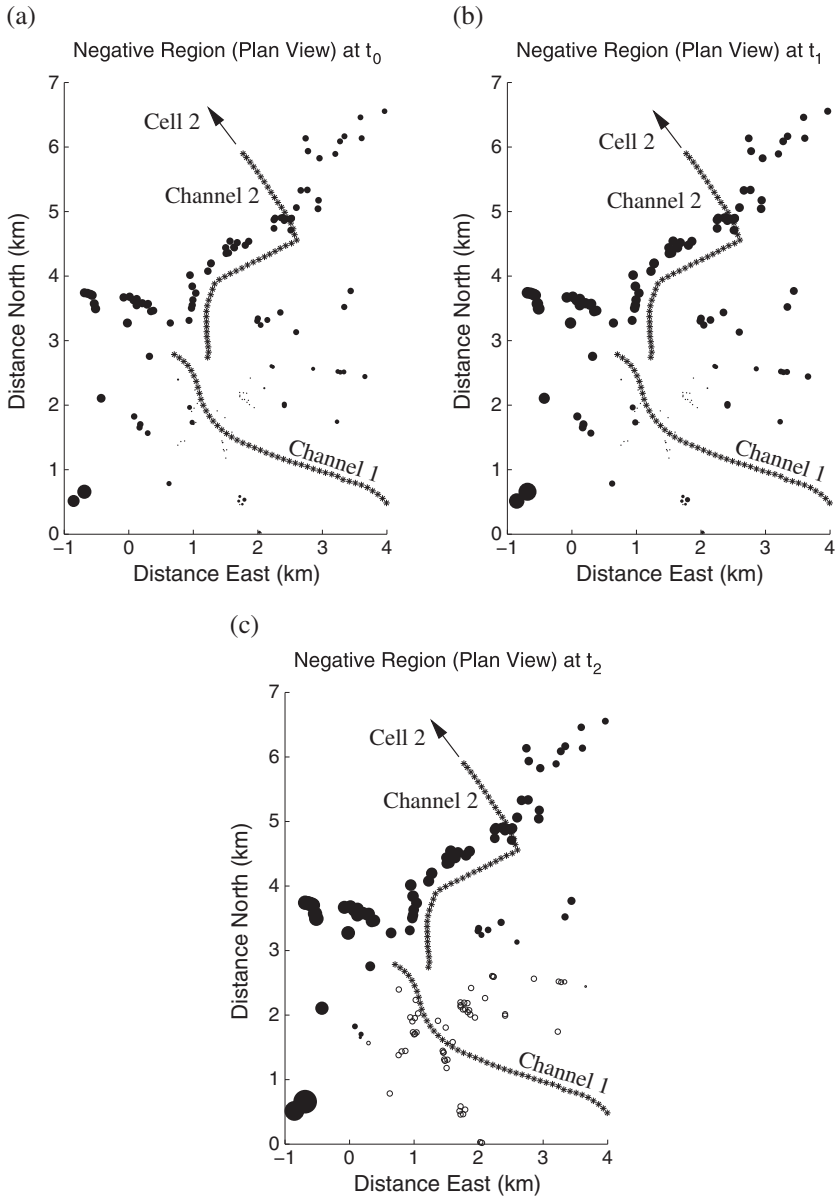

Figure 10. Plan view of the negative charge removed below 8 km altitude: (a) 23:05:42.023243 UT, (b) 23:05:42.1 UT, and (c) 23:05:42.3 UT. The area of each circle, centered on an LMA source, is proportional to charge amplitude. The circle is filled at a location where negative charge was removed, while the circle is open at a location where negative charge was deposited. The asterisks show the location of the channels in the positive region. At the time of Figure 10c, –15.6 C charge has been transported along channel 1, while –6.8 C was moved to a lower positive region corresponding to the open circles in a neighborhood of channel 1.

to the times t_0 and t_1, all the circles are all filled since negative charge was removed from the negative region. In Figures 10c) and 11c, which corresponds to the time t_2 after the K-changes, there are both open and filled circles since negative charge was both removed and deposited.

[61] These figures show that charge is initially drained along a northeasterly line which is mostly beneath channel 2 and parallel to channel 2 in the plan view. As the LMA sources along channel 2 propagate to the northeast, their altitude increases while the altitude of the LMA sources in the negative region below channel 2 decreases (see Figure 2b, the altitude plot). When the vertical separation between the LMA sources in the negative and positive regions reaches about 2 km, the propagation direction makes an abrupt left turn toward cell 2, which is about 5 km to the northwest. Hence, the initial charge transport, which took charge from the negative region beneath channel 2 and deposited it along channel 1, apparently led to breakdown along channel 2 without measurable charge transport along channel 2. Channel 2 initially mirrored the charge removal location as seen in Figure 10. Figure 10c shows that during the K-processes, negative charge on the upper left side of the figure was moved to a region beneath channel 1 (lower right side). Based on this charge movement, we conclude that the

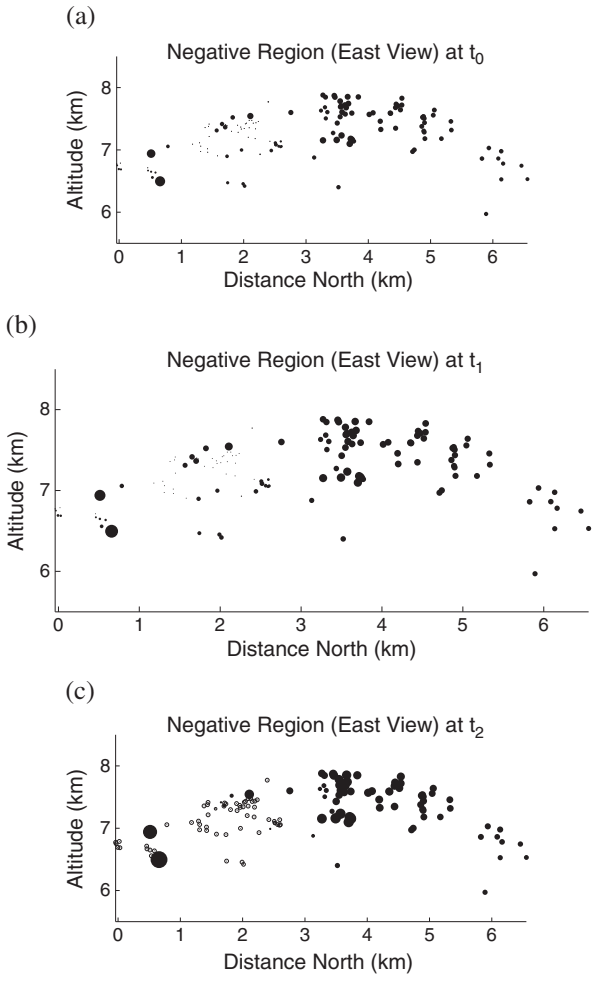

Figure 11. Charge movement below 8 km altitude: (a) 23:05:42.023243 UT, (b) 23:05:42.1 UT, and (c) 23:05:42.3 UT. The view is from the west looking toward the east. The area of each circle, centered on an LMA source, is proportional to charge amplitude. The circle is filled at a location where negative charge was removed, while the circle is open at a location where negative charge was deposited. At the time of Figure 11c, –15.6 C charge was transported along channel 1, while –6.8 C was moved to a positive region corresponding to the open circles.

region beneath channel 1 corresponding to the open circles in Figure 10c is *positively charged*.

[62] The possibility of low positive charges beneath channel 1 is consistent with observations in *Hager et al.* [2010]. In *Hager et al.* [2010, Figure 31], it is seen that between 10 and 20 km away from an updraft for a 2004 summer storm near Langmuir Laboratory, the mean altitude of the positive charge in an IC ranged from 6.5 to 7.2 km. Since channel 1 is about 15 km from the cells of Figure 1, it is possible that the LMA sources in the lower left side of Figure 3a (altitude between 6.5 and 7.5 km) are actually situated in a positive region, while the LMA sources in the lower right side are clearly in a negative region that was the source of charge for the flash. This complex charge structure is consistent with the complex layering of charges seen in balloon soundings of thunderstorms [*Marshall and Rust*, 1991, 1993; *Stolzenburg and Marshall*, 1994; *Stolzenburg et al.*, 1994, 1998a, 1998b, 1998c, 2001, 2002].

6. K-Changes

[63] We now analyze in more detail the charge transport during the K-changes that occur between t_1 and t_2 at about 23:05:42.124 UT, 23:05:42.211 UT, and 23:05:42.227 UT. We refer to these K-changes as K1, K2, and K3, respectively. Papers focusing on the measurement and study of K-changes include work by *Rhodes and Krehbiel* [1989], *Rakov et al.* [1992], *Rakov et al.* [1996], *Mazur et al.* [1995], *Shao et al.* [1995], and *Thottappillil et al.* [1990]. For a history of the literature, see *Rakov and Uman* [2003, pp. 182–188]. Rakov and Uman point out that the first inference concerning the K-process mechanism was made by *Malan and Schonland* [1951] who state that they are the result of "a small readjustment of charge within the cloud."

[64] The K-change refers to the abrupt steplike change in the electric field while the K-process also includes the events leading up to the steplike change in the electric field. For our flash, the K-process begins at about 23:05:42.086007 UT,

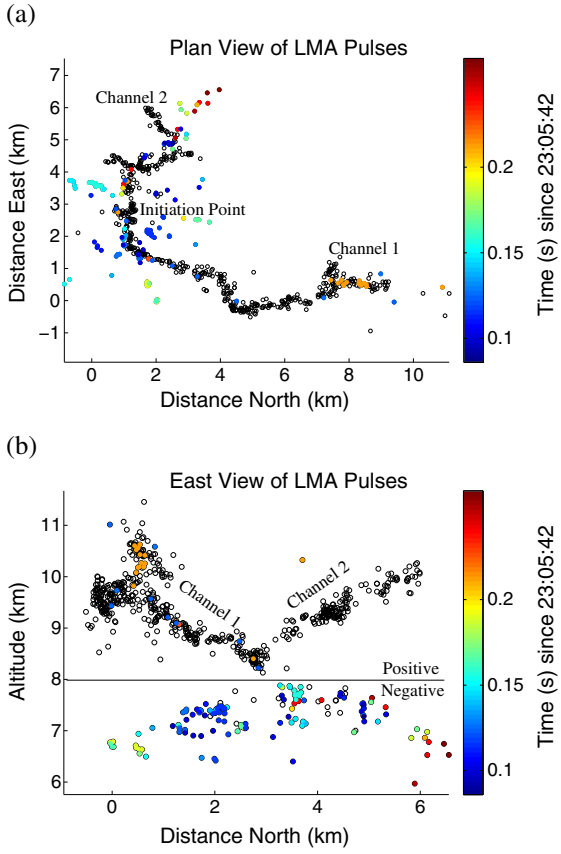

Figure 12. (a) Plan view of the LMA sources. (b) View from the west, looking east. The open circles show all the LMA sources while the colored dots show the LMA sources associated with the K-processes. The K-processes start with darker blue sources beneath 8 km. K1 corresponds to the light blue sources propagating to the end of channel 1. K2 corresponds to the green and yellow sources beneath 8 km, and orange sources propagating to the end of channel 1. K3 corresponds to the red dots.

Table 5. Comparison Between Modeled and Measured Fields for K-changes

	K1		K2	
	Measured	Modeled	Measured	Modeled
EG_z (kV/m)	–0.30	–0.25	–0.14	–.13
EF_x (kV/m)	2.95	2.92	2.56	2.55
EF_y (kV/m)	3.67	3.73	2.86	2.90
EF_z (kV/m)	–2.07	–1.96	–1.81	–1.74
Q_1 (C)		–0.80		–0.48
$\lvert Q_- \rvert$ (C)		2.40		1.77

shortly after the LMA sources reach the end of channel 2. The LMA sources associated with the K-processes are plotted in Figure 12. The K-changes correspond to the light blue dots (K1), the orange dots (K2), and the red dots (K3). Before each K-change, there was a sequence of LMA sources beneath 8 km altitude corresponding to colors in the spectrum that precede the color of the dots in the K-change itself.

[65] We now use the smooth charge transport model developed in section 5 to analyze the charge transport associated with the K-processes. In performing the fits, we restrict the charge transport in the negative region to the location of LMA sources associated with each K-change, and we set $\ell_i = -\infty$ for $i \in$ neg; by taking $\ell_i < 0$, this means that negative charge can be both transported down channel 1 and moved to a different location below 8 km (which we just observed also contains positive charge). With these adjustments, the model of section 5 is able to fit K1 and K2, as shown in Table 5, with a relative error between the modeled and measured electric fields around 2%. For K3, the best fit had a relative error around 30% with the error mostly concentrated in the z component of the electric field. We do not show results for K3 since we were unable to reconstruct the charge transport.

[66] In Figure 13, we plot the linear charge density along channel 1 associated with K1 and K2. K1 uniformly deposits charge in a distributed fashion along the channel. K2 appears to run out of charge before reaching the end of channel 1. For either of these K-changes, most of the charge transport occurs in the region beneath 8 km altitude. Comparing Q_1 to $|Q_-|$, the magnitude of the charge rearrangement below 8 km altitude was (2.40 – 0.80) C = 1.60 C for K1 and (1.77 – 0.48) C = 1.29 C for K2.

[67] In Figures 14 and 15, we show the charge rearrangement in the negative region. The charges are centered at the LMA sources; dark blue sources occurred first while dark red sources occurred last. The area of each circle is proportional to the charge amplitude. The circle has a black edge if negative charge was deposited at that location, while a circle without a black edge is a source of negative charge. Typically, LMA sources correspond to negative polarity breakdown through positive charge since positive polarity breakdown through negative charge produces far fewer LMA sources. Hence, according to the LMA record, the negative charge should tend to flow from blue colored dots toward red colored dots. Observe that the reconstructed charge transport is roughly consistent with the LMA data. That is, there are red and yellow circles with black edges indicating that negative charge was deposited at those location, while there are blue circles without

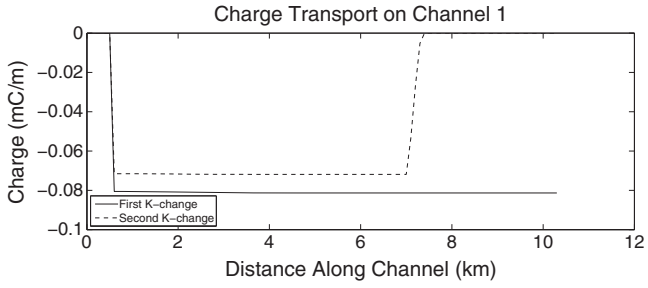

Figure 13. The linear charge density on channel 1 as a function of distance along the channel for the K-changes.

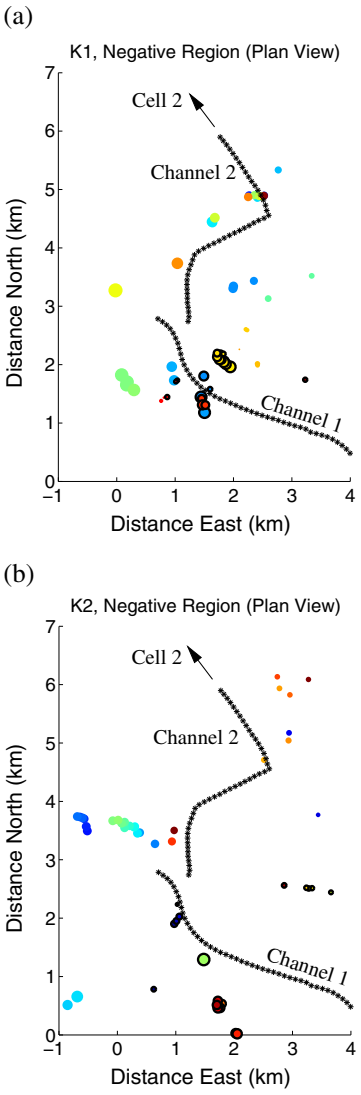

Figure 14. Plan view of the negative charge removed below 8 km altitude during the K-changes: (a) K1 and (b) K2. The area of each circle, centered on an LMA source, is proportional to charge amplitude. The circle has a black edge if negative charge was deposited at that location, while the circles without a black edge are the source of negative charge. The color of the circle is based on the time of the LMA source; the earliest sources are dark blue and the latest sources are dark red.

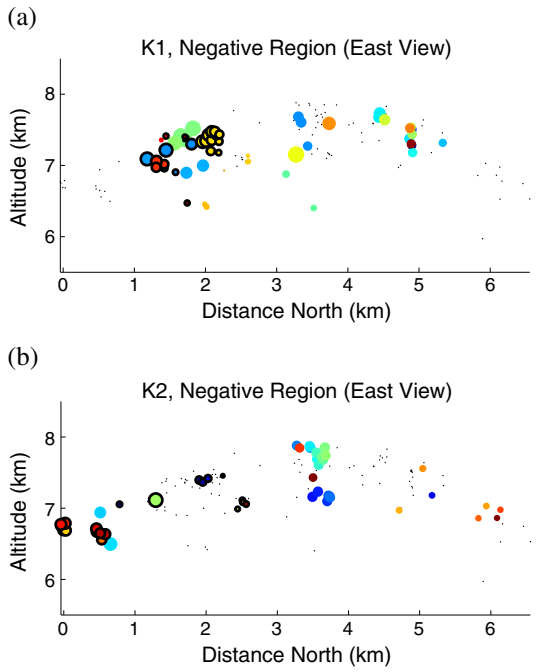

Figure 15. Negative charge removed below 8 km altitude during the K-changes: (a) K1 and (b) K2. The view is from the west looking toward the east. The area of each circle, centered on an LMA source, is proportional to charge amplitude. The circle has a black edge if negative charge was deposited at that location, while the circles without a black edge are the source of negative charge. The color of the circle is based on the time of the LMA source; the earliest sources are dark blue and the latest sources are dark red.

edges indicating that these locations were the origin of the negative charge.

[68] To conclude this section, we wish to make an observation concerning the speed of the charge transport process. *Winn et al.* [2011] computed the speed of the stepped-leader process associated with the initial charge transport and the K-changes using the propagation speed of the LMA sources. The average velocity of the stepped leader was 1.05×10^5 m/s while the average velocity of K1 when it was near the Esonde was 3.3×10^6 m/s.

[69] We can also estimate the relative propagation speeds using the electric field data. Since the Esonde records the electric field associated with a wave that approaches and passes the instrument, the time between different characteristics of the electric field wave could be compared to determine the relative propagation speeds of the waves. For example, let us compare the time between the first peak and the first trough in the y component of the electric field. For the stepped-leader process, this time difference is about 0.0222 s while for K1, this time difference is 0.0013 s. This implies that the current wave associated with K1 was moving about $0.0222/0.0013 \approx 17$ times faster than the stepped-leader current wave as it passed the Esonde. For comparison, the corresponding ratio based on the propagation speed of LMA sources was about 31. Note that in *Winn et al.* [2011], the velocity estimates gotten from the LMA sources ranged by factors of more than 2 depending on the specific LMA sources used to estimate speed.

7. Conclusions

[70] An intracloud flash on 24 August 2007 provided a unique opportunity for the analysis of lightning charge transport based on data from two Esondes near the flash, one about 300 m from the lightning channel. A dipole transport model did not fit the data since it neglected the channel charge near the flight Esonde. The uniform charge transport model provided an approximate fit to the data at 23:05:42.1 UT, but at 23:05:42.3 UT, after the K-changes were finished, there was a significant discrepancy between the best fitting uniform charge distribution and measurements. In particular, there was poor agreement with the Esonde on the ground, and the positive charge that was deposited along channel 2 was implausible.

[71] The fact that we could not fit the electric field data by a uniform charge distribution at 23:05:42.3 UT seems to indicate that late in the flash, the charge was not uniformly distributed on the channel. The smooth charge transport model allowed greater flexibility in choosing the charge amplitude, but not its location which was determined by the LMA sources. In the upper positive region, we required that negative charge be placed at the midpoints of segments forming the lightning channel. Beneath 8 km altitude, we required that charge be placed at the location of LMA sources. Penalties were used to create a smoothly varying charge density. With this additional flexibility, we obtained a very good fit to the measured electric field change shown in Table 4. The reconstructed charge distributions appear in Figures 9, 10, and 11.

[72] The charge transport analysis showed that during the initial 0.1 s of the IC, when the LMA first reached the end of channel 1 at time t_0, between 9 and 10 C, negative charge was deposited along channel 1, with about 3 C at the end of the channel, about 2 C near the start of the channel, and about 5 C along the channel as seen in Figure 9. During the next 0.027 s after the LMA reached the end of channel 1, another –5 or –6 C moved onto channel 1. This created a charge bulge near the start of channel 1 of about –3.6 C, and continued movement of charge toward the end of channel 1, as seen in the t_1 curve of Figure 9. During the subsequent K-changes, charge continued to move toward the end of channel 1 as indicated by the t_2 curve of Figure 9. In addition, during the K-processes, negative charge was transported to a positive region beneath channel 1 corresponding to the open circles in Figure 10c. As channel 1 cooled, each successive K-change deposited less charge on channel 1. According to Figure 13, the charge associated with K1 reached the end of the channel, while K2 appeared to run out of charge before reaching the end of the channel, and K3 stopped at the start of channel 1 according to the LMA data.

[73] After the transport was complete, about –5.8 C was located at the end of channel 1 and –1.8 C was located at the beginning of channel 1; –8.0 C was distributed along the channel with a linear charge density of about –0.90 mC/m. Hence, relative to the –15.6 C deposited along channel 1, 37% was deposited near the end of the channel, 11% was deposited near the beginning of the channel, and 51% was distributed along the channel.

[74] In the region beneath 8 km altitude, roughly –6.8 C was moved from a negatively charged region beneath channel 2 and deposited in a positive region beneath channel 1. Hence, out of the –22.4 C that was transported from the neg-

ative charge region, 30% of the charge was moved to a lower altitude beneath channel 1, while 70% was deposited along channel 1. This indicates that the region beneath 8 km is predominantly negatively charged, but with a significant pocket of positively charged particles.

[75] Although the IC contained two channels, the charge transport analysis showed that there was no measurable charge transport along channel 2. This result was surprising since the LMA sources forming channel 2 do not appear to be significantly different from the LMA sources forming channel 1. Nonetheless, there is additional strong physical evidence, besides the charge transport analysis, that there was no measurable charge transport down channel 2. It is important to remember that LMA sources correspond to a breakdown process, which may not produce significant charge transport. The post flash LMA burst discussed in section 2.2 contained 170 LMA sources, but there was no measurable change in the electric field and hence, no measurable charge transport. Additional evidence for the lack of measurable charge transport on channel 2 is provided by the analysis of *Winn et al.* [2011] of the stepped-leader recoils. As the stepped leader propagates to the end of the channel 1, recoils travel backward along the channel. The recoils correspond to an electric field wave which travels on the channel and passes within 200 or 300 m of the Esonde. When the recoil passes by the Esonde, it creates an oscillation or ripple which is superimposed on the measured electric field. The amplitude of these oscillations is on the order of kilovolts, even when the tip of the current pulse is 7 km from the Esonde. The oscillations associated with channel 2 should appear right after the dashed line marked "LMA reaches end channel 1" in Figure 6. The human eye cannot see the oscillations associated with the recoils of channel 2, but they are there, slightly above the noise. *Winn et al.* [2011] analyzed the recoils off the tip of the stepping leader for channel 2 (see their Section 8) and observed that the amplitude was an order of magnitude smaller than that of the recoils off the tip of the channel 1 leader, even though channel 2 is between 2 and 5 km from the Esonde. The amplitude of the oscillations in the electric field associated with the recoils should be proportional to the amplitude of the charge that lunges forward during a leader step. The small amplitude of the channel 2 recoil waves that pass by the Esonde seems to imply that the lunge in charge associated with the stepping leader for channel 2 is an order of magnitude smaller than the lunge in charge associated with the stepping leader of channel 1.

[76] Additional indications of negligible charge transport on channel 2 are the following: (a) The high altitude LMA pulses seen at the end of channel 1, that could correspond to streamers emerging from the end of channel 1, are missing from channel 2; in particular, the nine LMA sources that appear beyond the end of channel 2 in Figure 2b are low altitude sources around 6 km (blue dots). (b) There are no K-changes on channel 2, they only appear on channel 1. (c) The negative charge region discharged to the more distant channel 1 even though channel 2 is almost directly above much of the region where negative charge was discharged (see Figure 10).

[77] The accumulation of charge at the end of channel 1, which was needed to fit the data, does not make physical sense since a large amount of charge is concentrated in a small region near the end of the channel. Our interpretation of this charge buildup is that the charge is leaving the end of the channel through streamers and passing into the surrounding atmosphere. In Figure 2b there are six widely scattered LMA points at a high altitude (between 9060 and 11,320 m) east of the lightning channel. These LMA sources were each detected by eight LMA stations with reduced chi-squared values between 0.58 and 0.96, which is similar to the chi-squared values for the other sources in the flash. These relatively reliable LMA sources could be evidence of streamers extending from the end of the channel into the surrounding atmosphere. Channel 1 propagates toward cell 1 in Figure 1 which is expected to be a source for positive particles at relatively high altitude. Since the fit process constrains the charge to the channel, the best fit is gotten by putting charge near the end of the channel, as close as possible to the streamers. Possibly one reason that we were able to achieve good dipole fits to IC charge transport in *Hager et al.* [2007, 2010] was that the combined effect of the charge transported past the end of the main channel by streamers and the charge distributed along the channel was equivalent to a single charge deposit near the end of the channel.

[78] Charge transport was analyzed for the first two K-changes between 23:05:42.1 UT and 23:05:42.3 UT, while K3 could not be analyzed, possibly due to missing LMA sources. There were only nine LMA sources associated with the K3 process, while there were 58 and 49 associated with K1 and K2 processes, respectively. Due to the noise in the LMA data in 2007, we had to use a stringent acceptance criteria for a valid LMA source. The nine LMA sources associated with K3 that could be distinguished from the background noise did not have enough degrees of freedom to reproduce the measured electric field change.

[79] It was found that the K-changes transported some charge along channel 1, while most of the charge movement took place below 8 km altitude. The observation that the K-change transported some charge along channel 1 is consistent with previous literature such as that of *Shao and Krehbiel* [1996], *Akita et al.* [2010], and *Lu et al.* [2011]. In fact, the multidipole model of *Lu et al.* [2011] incorporates the LMA sources along the channel into the charge transport analysis. On the other hand, the charge deposits beneath 8 km was an unexpected discovery. Initially, it appeared that the region beneath 8 km altitude was a negative charge region. However, the analysis of the electric field change during the K-processes showed that the region beneath channel 1 corresponding to the open circles in Figure 10c was positively charged. The drop in the z component of the electric field at the Esonde from –9.4 kV/m before the K-changes to –17.1 kV/m after the K-changes is compelling evidence that negative charge was deposited beneath the Esonde during the K-changes. An analysis [*Hager et al.*, 2010] of another summer thunderstorm near Langmuir Laboratory found that the mean altitude of an IC's positive charge at a distance from 10 to 20 km from the updraft was between 6.5 and 7.2 km in altitude. Since channel 1 of our flash is about 15 km away from the main cells of our thunderstorm (see Figure 1), there is a potential for positively charged particles at the altitudes discovered in our analysis. Note that balloon soundings [*Marshall and Rust*, 1991, 1993; *Stolzenburg and Marshall*, 1994; *Stolzenburg et al.*, 1994, 1998a, 1998b, 1998c, 2001, 2002] often infer the potential for rather complex layering of charges in a thunderstorm.

[80] The charge transport analysis summarized in Figures 10 and 11 showed negative charge transported from beneath channel 2 (the filled circles in Figures 10c and 11c) to a region beneath channel 1 (the open circles). Roughly, the time sequence of the LMA sources was consistent with the flow of negative charge from the negative region to the lower positive region. In particular, in Figure 14, the yellow and red circles with black edges in the lower positive region (recipients of negative charge occurring late in the K-process) were preceded by earlier colors in the negative region without black edges (the source of the negative charge). Taking into account the upper and lower positive regions, the K-processes were fit by *tripoles* where charge was transported from the negative region to two distinct positive regions, one along the main lightning channel, and the other beneath the main lightning channel.

[81] In the smooth charge transport model, the tripolar transport mechanism was implemented by choosing $\ell_i < 0$ in the constraint $q_i \geq \ell_i$ for those i associated with LMA sources below 8 km altitude. Physically, this meant that negative charge could be moved from one location beneath 8 km to another location. This allowed us to rearrange charge beneath 8 km and achieve the tripole charge configuration. As seen in Table 3, without permitting the rearrangement of charge beneath 8 km altitude, the modeled vertical electric field at the Esonde was –13.6 kV/m while the measured vertical field was –17.1 kV/m at time t_2, the completion of the flash. The amplitude of the modeled vertical electric field needs to be increased almost 26% to agree with the measured field. By allowing the transport of charge from the negative region beneath channel 2 to a positive region beneath channel 1, the discrepancy between model and measurement was reduced to about 4%.

[82] Figure 13 shows that K1 deposited charge along all of channel 1, while K2 appears to run out of charge before reaching the end of channel 1. For CGs, K-changes are sometimes called "attempted leaders." In a sense, K2 attempted to reach the end of channel 1, but apparently not much of its charge reached the end of the channel; nonetheless, the LMA sources associated with K2 reached the end of channel 1. It was noted that the shape of the electric field profiles near the Esonde could be used to estimate the propagation speed of the K-change relative to the propagation speed of the stepped leader. This comparison indicated that the K1 current wave passed the Esonde about 17 times faster that the stepped-leader current wave.

[83] The charge transport analysis tells us where the negative charge originates and where it is deposited, but the path of channels beneath 8 km is less clear. Figures 3a and 10c may be the clearest pictures of the charge flow. During the first phase of the flash, negative charge flows from the filled circles of Figure 10c to channel 1, which roughly corresponds to flow from the lower right corner of Figure 3a to the upper left corner (channel 1). After –15.4 C has been transported at time t_1 in Table 4, a significant charge bulge has developed at the start of channel 1 as seen in Figure 9. During the K-processes, charge continues to flow up to the start of channel 1, but as channel 1 cools, less and less charge is transported down the channel by the K-changes (see Figure 13). At the same time, one or more new channels apparently develop to transport negative charge to the lower positive region corresponding to the open circles in Figure 10c. Possibly, the negative charge follows existing channels up to the start of channel 1, and then new channels down to the lower positive region. Thus, the charge bulge region at the beginning of channel 1 eventually became the initiation point for at least three channels, channel 1 and 2 and one or more channels to the lower positive region that was discharged by the K-processes.

[84] Channel 2 is a mystery. As explained earlier in this section, this channel does not transport measurable charge, and it only starts to form after –9.7 C has been transported from the negative region up to channel 1 (see column t_0 in Table 4). The effect of this charge transport and the neutralization of positive charge along channel 1 should be a decrease in electric field. Thus, it would appear that the development of channel 2 was not related to a growth of the ambient electric field in the vicinity of channel 2. On the other hand, the charge transport analysis shows a charge bulge developing at the start of channel 1. It appears that the neutralization of positive charge along channel 1 coupled with the increasing negative charge bulge at the start of channel 1 produced an increase in the electric field at the start of channel 1 in the direction of channel 2 which initiated the breakdown along channel 2. The path of channel 2 seems to initially mirror the filled circles in Figure 10 associated with the removal of negative charge. A possible explanation for the path of channel 2 is the following: The removal of negative charge along the curve of filled circles in Figure 10 exposed a lower positive region which initially guided the propagation of channel 2. When the separation between channel 2 and the exposed positive region became large enough, the positive charge at the top of cell 2 caused channel 2 to bend to the left in Figure 10.

[85] The connection between charge transport and the LMA sources is complex. There was no LMA activity in the negative region during the initial charge transport which implied positive polarity breakdown through negative charge, while the initial charge transport down channel 1 was accompanied by many LMA sources due to negative polarity breakdown through positive charge. After the initial charge transport, LMA sources propagated down channel 2, but without measurable charge transport. This was followed by K-changes in which LMA sources propagated into two different positive regions, an upper region along channel 1 and a lower region beneath channel 1. Finally, about 0.4 s after the completion of the flash, there were 170 LMA sources beneath all the previous LMA sources, but no measurable charge transport.

Appendix A: The Laplace Solver

[86] To implement the approach developed in section 4, we need to solve Laplace's equation over the surface of the earth. A fine mesh is needed near the instrument, while a coarse mesh is sufficient far from the instrument where the potential is small. This suggests that we should discretize Laplace's equation $\nabla^2 V = 0$ in a spherical coordinate system whose origin is at the center of the earth and whose z axis points through the instrument. Consider a rectangular coordinate system (x, y, z) and a related spherical coordinate system defined by the coordinates (ρ, θ, ϕ) where ρ is the distance to the origin (center of the earth), θ is the angle of rotation in the (x, y) plane ($\theta = 0$ corresponds to the x axis

and $\theta = \pi/2$ is along the y axis), and ϕ is the angle of rotation away from the z axis. Hence, $\phi = 0$ points along the z axis. The equations relating the spherical coordinates to the rectangular coordinates are

$$x = \rho \sin\phi \cos\theta, \quad y = \rho \sin\phi \sin\theta, \quad z = \rho \cos\phi.$$

The gradient in spherical coordinates is

$$\nabla = \hat{\boldsymbol{\rho}} \frac{\partial}{\partial \rho} + \hat{\boldsymbol{\theta}} \frac{1}{\rho \sin\phi} \frac{\partial}{\partial \theta} + \hat{\boldsymbol{\phi}} \frac{1}{\rho} \frac{\partial}{\partial \phi}.$$

Suppose that the domain of interest is subdivided in a mesh corresponding to

$$\rho_i,\ 1 \le i \le I, \quad \theta_j,\ 1 \le j \le J, \quad \phi_k,\ 1 \le k \le K.$$

We approximate the solution to Laplace's equation at the centroid of each volume element in the mesh. A typical volume element has the form

$$\left\{(\rho, \theta, \phi) : \rho_{i-1} \le \rho \le \rho_i, \quad \theta_{j-1} \le \theta \le \theta_j, \quad \phi_{k-1} \le \phi \le \phi_k\right\}.$$

The centroid $(\bar{\rho}_i, \bar{\theta}_j, \bar{\phi}_k)$ of the volume element is given by

$$\bar{\rho}_i = \frac{\rho_{i-1} + \rho_i}{2}, \quad \bar{\theta}_j = \frac{\theta_{j-1} + \theta_j}{2}, \quad \bar{\phi}_k = \frac{\phi_{k-1} + \phi_k}{2}.$$

We use the volume element approach developed by *Hager et al.* [1989]. This approach corresponds to integrating Laplace's equation over the volume element centered at $(\bar{\rho}_i, \bar{\theta}_j, \bar{\phi}_k)$. The integral has the approximation

$$\left(\sum_{l=1}^{3} C_l \partial_l^+ - \sum_{l=1}^{3} D_l \partial_l^- \right) V_{ijk} = 0,$$

where

$$\begin{array}{llll} \partial_1^+ V_{ijk} = \frac{V_{i+1,jk} - V_{ijk}}{\bar{\rho}_{i+1} - \bar{\rho}_i}, & \partial_2^+ V_{ijk} = \frac{V_{i,j+1,k} - V_{ijk}}{\bar{\theta}_{j+1} - \bar{\theta}_j}, & \partial_3^+ V_{ijk} = \frac{V_{ij,k+1} - V_{ijk}}{\bar{\phi}_{k+1} - \bar{\phi}_k}, \\ \partial_1^- V_{ijk} = \partial_1^+ V_{i-1,j,k}, & \partial_2^- V_{ijk} = \partial_2^+ V_{i,j-1,k}, & \partial_3^- V_{ijk} = \partial_3^+ V_{i,j,k-1}, \end{array}$$

and

$$\begin{array}{rcl} C_1 &=& 2(\theta_j - \theta_{j-1})\rho_i^2 \sin\bar{\phi}_k \sin(\phi_k - \phi_{k-1})/2, \\ D_1 &=& 2(\theta_j - \theta_{j-1})\rho_{i-1}^2 \sin\bar{\phi}_k \sin(\phi_k - \phi_{k-1})/2, \\ C_2 &=& \frac{1}{\sin\bar{\phi}_k}(\rho_i - \rho_{i-1})(\phi_k - \phi_{k-1}) = D_2, \\ C_3 &=& \sin\phi_k(\rho_i - \rho_{i-1})(\theta_j - \theta_{j-1}) \\ D_3 &=& \sin\phi_{k-1}(\rho_i - \rho_{i-1})(\theta_j - \theta_{j-1}) \end{array}$$

Analogous discretizations based on cylindrical and rectangular coordinate systems are given in *Hager et al.* [1989].

[87] The domain that we discretized extended from the surface of the earth to the ionosphere (taken as 100 km altitude) and radially a distance 100 km away from Langmuir Laboratory along the surface of the Earth. We considered a mesh of size 298 in the ρ direction, and 101 in the ϕ and θ directions. We grade the mesh so that near Langmuir Laboratory, the mesh elements have sides between 20 and 50 m, while 100 km away, the largest sides of mesh elements are around 4.5 km. We need to compute the potential at roughly three million ($298 \times 101 \times 101$) locations in the domain. The linear equations were solved using the CHOLMOD package [*Chen et al.*, 2009; *Davis and Hager*, 2009] developed in an earlier NSF grant. The discretized linear system was reordered using a fill reducing nested dissection ordering generated by METIS [*Karypis and Kumar*, 1998] leading to a symmetric, positive definite linear system, whose Cholesky factor contains 6.4×10^9 nonzero entries, which requires 51 GB to store. The factorization can be computed within an hour on a 12 core Dell T7500 workstation with 96 GB memory and Intel Xeon 5600 series processors operating at 3.47 GHz. The resulting factored linear systems, one for each LMA source and one for each channel segment, can be formed in MATLAB and solved with CHOLMOD at the rate of four per minute.

[88] In *Lu et al.* [2011], the authors took into account a realistic terrain based on data from the U.S. Geological Survey and they solved Poisson's equation for point charges using a commercial finite element package COMSOL. They were able to model a domain of size 80 km by 80 km by 40 km using a mesh with 600 m sides near Langmuir Laboratory and 10 km sides further away. Due to CPU limitations, the number of point charges was reduced to 11. The software based on our techniques described above allowed us to consider a 200 km by 200 km by 100 km domain, and meshes with sides between 20 and 50 m near Langmuir Laboratory and 4.5 km farther away. The solution time of four solves per minute meant that we could analyze the 289 point charges associated with this flash (137 in the negative region, 105 on channel 1, and 47 on channel 2) in about 1.2 h.

[89] **Acknowledgments.** This work was funded by grant 0724750 from the National Science Foundation. Additional funding was provided by the Irving and Marion Langmuir bequest to Langmuir Laboratory. The field operations at Langmuir Laboratory were conducted on the Cibola National Forest under a Special Use Permit from the U.S. Forest Service. The authors gratefully acknowledge comments from William P. Winn on an early draft of the paper. His suggestions concerning notation, conventions, and presentation significantly improved the paper. Also, a comment from Paul R. Krehbiel concerning the need for a deeper analysis of K-changes was much appreciated. This led to the inclusion of section 6. Stimulating comments and suggestions by Edward Mansell, that played a key role in the final shaping of the paper, are gratefully acknowledged. The data used in this paper were provided by Richard G. Sonnenfeld. Finally, the authors appreciate the detailed comments and suggestions of the reviewers which improved the paper.

References

Adlerman, E. J., and E. R. Williams (1996), Seasonal variation of the global electrical circuit, *J. Geophys. Res.*, *101*, 29,679–29,688.

Akita, M., Y. Nakamura, S. Yoshida, T. Morimoto, T. Ushio, Z. Kawasaki, and D. Wang (2010), What occurs in K process of cloud flashes?, *J. Geophys. Res.*, *115*, D07106, doi:10.1029/2009JD012016.

Chen, Y., T. A. Davis, W. W. Hager, and S. Rajamanickam (2009), Algorithm 887: CHOLMOD, supernodal sparse Cholesky factorization and update/downdate, *ACM Trans. Math. Softw.*, *35*.

Coleman, L. M., T. C. Marshall, M. Stolzenburg, T. Hamlin, P. R. Krehbiel, W. Rison, and R. J. Thomas (2003), Effects of charge and electromagnetic potential on lightning propagation, *J. Geophys. Res.*, *108*(D9), 4298, doi:10.1029/2002JD002718.

Davis, T. A., and W. W. Hager (2009), Dynamic supernodes in sparse Cholesky update/downdate and triangular solves, *ACM Trans. Math. Softw.*, *35*.

Few, A. A. (1970), Lightning channel reconstruction from thunder measurements, *J. Geophys. Res.*, *75*, 7517–7523.

Hager, W. W., J. S. Nisbet, and J. R. Kasha (1989), The evolution and discharge of electric fields within a thunderstorm, *J. Comput. Phys.*, *82*, 193–217.

Hager, W. W., R. G. Sonnenfeld, B. C. Aslan, G. Lu, W. P. Winn, and W. L. Boeck (2007), Analysis of charge transport during lightning using balloon borne electric field sensors and LMA, *J. Geophys. Res.*, *112*, D18204, doi:10.1029/2006JD008187.

Hager, W. W., B. C. Aslan, R. G. Sonnenfeld, T. D. Crum, J. D. Battles, M. T. Holborn, and R. Ron (2010), Three-dimensional charge structure of a mountain thunderstorm, *J. Geophys. Res.*, *115*, D12119, doi:10.1029/2009jd013241.

Hager, W. W., et al. (2012), Charge rearrangement by sprites over a north Texas mesoscale convective system, *J. Geophys. Res.*, *117*, D22101, doi:10.1029/2012JD018309.

Jacobson, E. A., and E. P. Krider (1976), Electrostatic field changes produced by Florida lightning, *J. Atmos. Sci.*, *33*, 103–117.

Karypis, G., and V. Kumar (1998), A fast and high quality multilevel scheme for partitioning irregular graphs, *SIAM J. Sci. Comput.*, *20*, 359–392.

Koshak, W. J., and E. P. Krider (1989), Analysis of lightning field changes during active Florida thunderstorms, *J. Geophys. Res.*, *94*, 1165–1186.

Koshak, W. J., and E. P. Krider (1994), A linear method for analyzing lightning field changes, *J. Atmos. Sci.*, *51*, 473–488.

Koshak, W. J., E. P. Krider, and M. J. Murphy (1999), A multipole expansion method for analyzing lightning field changes, *J. Geophys. Res.*, *104*, 9617–9633.

Krehbiel, P. R. (1981), An analysis of the electric field change produced by lightning, Ph.D. thesis, Univ. of Manchester Inst. of Scie. and Technol., Manchester, England.

Krehbiel, P. R. (1986), The electrical structure of thunderstorms, in *The Earth's Electrical Environment*, pp. 90–113, National Academy Press, Washington, D. C.

Krehbiel, P. R., M. Brook, and R. A. McCrory (1979), An analysis of the charge structure of lightning discharges to ground, *J. Geophys. Res.*, *84*, 2432–2456.

Liu, X., and P. R. Krehbiel (1985), The initial streamer of intracloud lightning flashes, *J. Geophys. Res.*, *90*, 6211–6218.

Lu, G., W. P. Winn, and R. G. Sonnenfeld (2011), Charge transfer during intracloud lightning from a time-dependent multidipole model, *J. Geophys. Res.*, *116*, D03209, doi:10.1029/2010JD014495.

Malan, D. J., and B. F. J. Schonland (1951), The distribution of electricity in thunderclouds, *Proc. R. Soc., Ser. A*, *209*, 158–177.

Marshall, T. C., and W. D. Rust (1991), Electric field soundings through thunderstorms, *J. Geophys. Res.*, *96*, 22,297–22,306.

Marshall, T. C., and W. D. Rust (1993), Two types of vertical electrical structures in stratiform precipitation regions of mesoscale convective systems, *Bull. Am. Meteorol. Soc.*, *74*, 2159–2170.

Mazur, V., and L. H. Ruhnke (1998), Model of electric charges in thunderstorms and associated lightning, *J. Geophys. Res.*, *103*, 23,299–23,308.

Mazur, V., P. R. Krehbiel, and X.-M. Shao (1995), Correlated high-speed video and radio interferometric observations of a cloud-to-ground lightning flash, *J. Geophys. Res.*, *100*, 25,731–25,753.

Murphy, M. J., E. P. Krider, and M. W. Maier (1996), Lightning charge analyses in small Convection and Precipitation Electrification (CaPE) experiment storms, *J. Geophys. Res.*, *101*, 29,615–29,626.

Proctor, D. E. (1981), VHF radio pictures of cloud flashes, *J. Geophys. Res.*, *86*, 4041–4071.

Proctor, D. E. (1997), Lightning flashes with high origins, *J. Geophys. Res.*, *102*, 1693–1706.

Rakov, V. A., and M. A. Uman (2003), *Lightning Physics and Effects*, Cambridge Univ. Press, Cambridge.

Rakov, V. A., R. Thottappillil, and M. A. Uman (1992), Electric field pulses in K and M changes of lightning ground flashes, *J. Geophys. Res.*, *97*, 9935–9950.

Rakov, V. A., M. A. Uman, G. R. Hoffman, M. W. Masters, and M. Brook (1996), Electric field pulses in K and M changes of lightning ground flashes, *IEEE Trans. Electromagn. Compat.*, *38*, 156–164.

Rhodes, C. T., and P. R. Krehbiel (1989), Interferometric observations of a single stroke cloud-to-ground flash, *Geophys. Res. Lett.*, *16*, 1169–1172.

Rison, W., R. J. Thomas, P. R. Krehbiel, T. Hamlin, and J. Harlin (1999), A GPS-based three-dimensional lightning mapping system: Initial observations in central New Mexico, *Geophys. Res. Lett.*, *26*, 3573–3576.

Schonland, B. F. J. (1956), The lightning discharge, in *Handbuch der Physik*, vol. 22, edited by S. Flügge, pp. 576–628, Springer-Verlag, Berlin.

Shao, X. M., and P. R. Krehbiel (1996), The spatial and temporal development of intracloud lightning, *J. Geophys. Res.*, *101*, 26,641–26,668.

Shao, X. M., P. R. Krehbiel, R. J. Thomas, and W. Rison (1995), Radio interferometric observations of cloud-to-ground lightning phenomena in Florida, *J. Geophys. Res.*, *100*, 2749–2783.

Sonnenfeld, R. G., J. Battles, G. Lu, and W. P. Winn (2006), Comparing E-field changes aloft to lightning mapping data, *J. Geophys. Res.*, *111*, D20209, doi:10.1029/2006JD007242.

Stolzenburg, M., and T. C. Marshall (1994), Testing models of thunderstorm charge distributions with Coulomb's law, *J. Geophys. Res.*, *99*, 25,921–25,932.

Stolzenburg, M., T. C. Marshall, W. D. Rust, and B. F. Smull (1994), Horizontal distribution of electrical and meteorological conditions across the stratiform region of a mesoscale convective system, *Mon. Wea. Rev.*, *122*, 1777–1797, MWR Special Issue.

Stolzenburg, M., W. D. Rust, and T. C. Marshall (1998a), Electrical structure in thunderstorm convective regions 2. Isolated storms, *J. Geophys. Res.*, *103*, 14,079–14,096.

Stolzenburg, M., W. D. Rust, and T. C. Marshall (1998b), Electrical structure in thunderstorm convective regions 3. Synthesis, *J. Geophys. Res.*, *103*, 14,097–14,108.

Stolzenburg, M., W. D. Rust, B. F. Smull, and T. C. Marshall (1998c), Electrical structure in thunderstorm convective regions 1. Mesoscale convective systems, *J. Geophys. Res.*, *103*, 14,059–14,078.

Stolzenburg, M., T. C. Marshall, and W. D. Rust (2001), Serial soundings of electric field through a mesoscale convective system, *J. Geophys, Res.*, *106*(D12), 12,371–12,380.

Stolzenburg, M., T. C. Marshall, W. D. Rust, and D. L. Bartels (2002), Two simultaneous charge structures in thunderstorm convection, *J. Geophys. Res.*, *107*(D18), 4352, doi:10.1029/2001JD000904.

Thomas, R. J., P. R. Krehbiel, W. Rison, T. Hamlin, J. Harlin, and D. Shown (2001), Observations of VHF source powers radiated by lightning, *Geophys. Res. Lett.*, *28*, 143–146.

Thomas, R. J., P. R. Krehbiel, W. Rison, S. J. Hunyady, W. P. Winn, T. Hamlin, and J. Harlin (2004), Accuracy of the lightning mapping array, *J. Geophys. Res.*, *109*, D14207, doi:10.1029/2004JD004549.

Thottappillil, R., V. A. Rakov, and M. A. Uman (1990), K and M changes in close lightning ground flashes in Florida, *J. Geophys. Res.*, *95*, 18,631–18,640.

Weber, M. E., H. J. Christian, A. A. Few, and M. F. Stewart (1982), A thundercloud electric field sounding: Charge distribution and lightning, *J. Geophys. Res.*, *87*, 7158–7169.

Wilson, C. T. R. (1916), On some determinations of the sign and magnitude of electric discharges in lightning flashes, *Proc. R. Soc. Ser. A*, *92*, 555–574.

Wilson, C. T. R. (1920), III. Investigations on lightning discharges and on the electric field of thunderstorms, *Phil. Trans. R. Soc., Ser. A*, *221*, 73–115.

Winn, W. P., G. D. Aulich, S. J. Hunyady, K. B. Eack, H. E. Edens, P. R. Krehbiel, W. Rison, and R. G. Sonnenfeld (2011), Lightning leader stepping, K changes, and other observations near an intracloud flash, *J. Geophys. Res.*, *116*, D23115, doi:10.1029/2011JD015998.

Workman, E. J., and R. E. Holzer (1939), Quantities of charge transfers in lightning discharges, *Phys. Rev.*, *55*, 598.